Identification of extreme precipitation threat across midlatitude regions based on short-wave circulations

Shih-Yu Wang[12], Robert E. Davies[1], and Robert R. Gillies[12]

1. Utah Climate Center, Utah State University, Logan, UT

2. Department of Plants, Soils, and Climate, Utah State University, Logan, UT

May 2013

August 2013

September 2013

Corresponding author: Dr. S.-Y. Simon Wang, 4820 Old Main Hill, Logan, UT 84322

E-mail: simon.wang@usu.edu

Abstract

The most severe thunderstorms, producing extreme precipitation, occur over subtropical and midlatitude regions. Atmospheric conditions conducive to organized, intense thunderstorms commonly involve the coupling of a low-level jet (LLJ) with a synoptic short wave. The midlatitude synoptic activity is frequently modulated by the circumglobal teleconnection (CGT) – in which meridional gradients of the jet stream act as a guide for short Rossby waves. Previous research has linked extreme precipitation events with either the CGT or the LLJ, but has not linked the two circulation features together. In this study, a circulation-based index was developed by combining (a) the degree of the CGT and LLJ coupling, (b) the extent to which this CGT-LLJ coupling connects to regional precipitation, and (c) the spatial correspondence with the CGT (short-wave) trending pattern over the most recent 32 years (1979-2010). Four modern-era global reanalyses, in conjunction with four gridded precipitation datasets, were utilized to minimize spurious trends. The results are suggestive of a link between several recent extreme precipitation events and the CGT/LLJ trends, including those leading to the 2008 Midwest flood in U.S., the 2011 tornado outbreaks in southeastern U.S., the 2010 Queensland flood in northeastern Australia and the 2010 Pakistan flood. Moreover, an analysis of three CMIP5 models from the historical experiments points to the role of greenhouse gases in forming the CGT trends during the warm season.

1. Introduction

Recent devastating floods such as those in the central U.S. (June 2008 “Midwest flood”), in Pakistan (July-August 2010), in eastern Australia (December 2010 “Queensland flood”), and in Brazil (January 2011) have resulted in tremendous societal and economic losses. None of these floods were caused by tropical cyclones and yet, each of the extreme precipitation events was unprecedented in its particular region, not only in the scale of damage but in the magnitude of precipitation that initiated the flooding. Increased extremes in precipitation worldwide have been observed and in many cases have been attributed to increased greenhouse gas (GHG) loadings in the atmosphere leading to moisture intensification (Easterling et al. 2000; Diffenbaugh et al. 2005; O'Gorman and Schneider 2009; among others). However, the current understanding of extreme precipitation events remains insufficient for climate prediction to operationally provide an accurate probabilistic assessment as to where and when extreme events will most likely occur. The purpose of this paper is to develop a method of identifying high-threat regions of extreme precipitation under the changing climate.

Satellite observations such as the Tropical Rainfall Measuring Mission (TRMM) have confirmed that the most intense thunderstorms occur over subtropical and/or semiarid regions, rather than over the heavy-raining tropics (Zipser et al. 2006). Correspondingly, there are relatively more extreme precipitation events, as well as steeper increases in their magnitude, over the subtropics than the tropics (e.g., Sun et al. 2007; Sugiyama et al. 2010). The atmospheric conditions conducive to intense convective storms usually involve strong vertical shear, a low-level jet (LLJ), and synoptic forcing by propagating short waves. When they occur in unison, these conditions provide the key ingredients for organized convection: instability, moisture and lift (Doswell 2001). In other words, the observed increase in extreme precipitation likely has occurred in conjunction with certain changes in those factors. Organized convective storms often take place in regions where the tropical moist air meets the midlatitude continental/polar air, with the former providing conditional instability and the latter generating frontal lift. Regions of active mesoscale convective systems (MCSs), for example, are often regions of frequent, diurnally-varying LLJs as well (Stensrud 1996; Monaghan et al. 2010). When the evolution of the LLJ is coupled with the propagation of upper-level short waves (referred as the 300-hPa level in Uccellini 1980), the resulting MCSs tend to be stronger and more organized, such as those forming the mesoscale convective complex (Maddox 1980, 1983). Extreme precipitation events worldwide are almost always a result of consecutive occurrences of these strong and organized MCSs (Tetzlaff et al. 2012).

Around the world, regions where tropical and midlatitude air masses interact correspond to the positions of the jet streams. The meridional gradients of the jet streams and their nearly circumpolar extent act as a guide for short Rossby waves (Hoskins and Ambrizzi 1993), a dynamical process referred to as the circumglobal teleconnection (CGT). One commonly accepted mechanism of the CGT is Rossby wave propagation, in which the jet stream acts as a waveguide to provide an important source of circumglobal teleconnectivity, particularly in winter (Hoskins and Ambrizzi 1993; Branstator 2002). The CGT connects climate anomalies between widely separated regions within similar latitude zones through Rossby wave energy dispersion induced by local vorticity sources (Schubert et al. 2011). The CGT occurs with a preferred zonal wave-5 structure with its wave amplitudes confined within the jet streak. Although the intensity of the CGT is stronger at the upper levels (e.g., between 200-300 hPa), the circulation anomaly exhibits a vertically uniform (or barotropic) structure (Wang et al. 2010). Variability of the CGT is uncorrelated with the El Niño-Southern Oscillation (ENSO), but might be connected to the North Atlantic Oscillation (Branstator 2002; Ding and Wang 2005; Yasui and Watanabe 2010). The CGT can also occur in summer (Ding and Wang 2005) and spring transition seasons (Wang et al. 2010), as the meridional gradients and nearly circumpolar extent of the summer jets form important guides for Rossby waves as well. Further evidence has been found that, the summertime CGT has stronger variability in the subseasonal timescale than the interannual one (Ding and Wang 2007; Wang et al. 2010; Schubert et al. 2011) – this feature is directly relevant to extreme precipitation events that tend to persist for an extended period of time.

There has been considerable evidence of the linkage between the CGT and regional climate extremes. For instance, in the central United States, the anomalous circulation with predominant short-wave features modulates summer precipitation (Lau and Weng 2002) and the Great Plains LLJ (Weaver and Nigam 2008). Similar CGT modulations on regional climate extremes have been observed over the past decade, including northern India (Ding and Wang 2005, 2007), Pakistan (Wang et al. 2011b), East Asia (Krishnan and Sugi 2001), Eurasia (Matsueda 2011; Schubert et al. 2011), and the western United States (Wang et al. 2010). The CGT modulation on regional climate also exists in the Southern Hemisphere (Ambrizzi et al. 1995) affecting South America (Junquas et al. 2012).

Post-1970s climate change has modified the atmospheric general circulation in two fundamental ways: (a) a weakening and a poleward shift of the jet streams (Archer and Caldeira 2008) leading to potentially further meandering of the jet (Rivière 2011), and (b) a widening of the tropical belt and expansion of the Hadley circulation (Seidel et al. 2008; Lu et al. 2009). Given the CGT's underlying waveguide mechanism, any long-term changes in the jet stream may affect the stationary wave train and, in turn, modify the CGT characteristics. Indeed, recent studies (Wang et al. 2011b; Francis and Vavrus 2012; Screen and Simmonds 2013) have found an increase in the amplitude of larger zonal wavenumbers (i.e. short stationary waves) along the midlatitudes. Likewise, the widened tropical belt increases the moisture and strengthens the moisture flux towards the midlatitudes; one such response is the enhanced transport of moisture by the LLJ as has been observed in the U.S. Great Plains (Cook et al. 2008; Weaver et al. 2009). Therefore, in regions where increased moisture transport of the enhanced LLJ interacts with increased transient vorticity source associated with the CGT, the combined increases in moisture and lift are conducive to deep, moist convection. These processes, together with warming in the lower troposphere that decreases static stability and holds more moisture (e.g., Gaffen et al. 2000), could enhance the likelihood for extreme precipitation events over those particular regions.

In order to identify such regions, we developed a technique to diagnose the trend in extreme precipitation threat under the changing climate and its geographical distribution. This technique characterizes the CGT and LLJ dynamics using a set of circulation criteria and regression analyses. The purpose of this analysis is to provide a circulation-based evaluation for global climate models without directly engaging simulated precipitation, which remains considerably biased. The long-term trend of the circulations was examined through an ensemble of modern-era global reanalyses; these are introduced in

Section 2. Evidence of the enhanced CGT and the analysis procedure are explained in Section 3. Interpretation of the diagnostics and the mapping results of precipitation threat are presented in Section 4. Possible cause of the changing CGT effects is discussed in Section 5. A conclusion from the results is summarized in Section 6.

2. Data Sources

Global reanalysis datasets provide complete coverage over most geographical regions around the world. However, trend analysis using a single reanalysis has led to concerns related to changing observation systems that may introduce spurious trends (Paltridge et al. 2009). Thus, to obtain a reliable or optimal estimate of any long-term trend, we utilized an array of global reanalyses and sought consensus. For the global reanalysis we used four post-1979 datasets that cover the satellite era: MERRA (Rienecker et al. 2011), CFSR (Saha et al. 2010), ERA-Interim (Dee et al. 2011) and the JRA-25 (Onogi et al. 2007); the acronyms, full names, and description of each dataset are provided in Table 1. Previous studies have also raised concerns about the quality of gridded precipitation data over data-poor regions (e.g., Ghosh et al. 2009). Thus, for the gridded precipitation datasets we used the satellite-enhanced GPCP (Adler et al. 2003) and CMAP (Xie and Arkin 1997) data combined for the global domain, the GPCC (http://gpcc.dwd.de/) and PREC/L (Chen et al. 2002) data combined overland (owing to their higher spatial resolution), leading to four precipitation data averaged overland at a 2.5° resolution and two over ocean (equally weighted). Again the acronyms, full names, and spatial resolution of the precipitation data are provided in Table 1. All the aforementioned reanalysis and precipitation datasets are for monthly means. For daily precipitation we used the Climate Prediction Center (CPC) Daily Unified precipitation data at a 0.5° resolution (http://www.esrl.noaa.gov/psd/data/gridded/data.unified.html).

In an attempt to attribute the cause of the observed changes in circulation patterns, we examined three climate models that participated in the Coupled Model Intercomparison Project (CMIP5; Taylor et al. 2011): the CNRM, GISS, and CanESM models (see Table 1 for full names). These three models were chosen since each has a distinct jet stream bias (further explained in Section 5). For the attribution analysis, we used two sets of the CMIP5 Historical Single-Forcing Experiments, driven by (a) natural forcing only (Natural, including solar and volcano) and (b) greenhouse gas forcing only (GHG). Each experiment produced a five-member ensemble, initialized from long-stable preindustrial (year 1850) control settings up to year 2005 (Taylor et al. 2011).

Storm reports consisting of gusty winds and hail were compiled by the Storm Prediction Center (SPC) at the Storm Data publication website (http://www.spc.noaa.gov/climo/historical.html). Bias and quality problems inherent in storm data included marked increases in weaker wind and hail reports over the last few decades, due largely to human and population biases (e.g., Weiss 2002). We detrended the data to remove such biases. Following Wang et al. (2011a), in this study we projected wind gusts greater than 50 knots and hail with 3/4 inch in diameter or greater onto a 2°x 2° grid mesh, and then accumulated these reports over a 24-hour interval for each day. This procedure generated "convective wind and hail frequencies" over the continental United States and designated our criteria for severe weather.

3. Analysis Procedure

a. Change in the CGT pattern

The CGT typically features a zonal wave-5 pattern confined to the mean jet (Branstator 2002; Ding and Wang 2005); this justifies the use of spatial harmonic analysis in filtering the circulations in order to obtain the CGT signal (following Wang et al. 2010). In addition, the spatial filtering helps isolate climate patterns induced from widespread tropical Pacific forcings, such as ENSO (or ENSO-like decadal variations), which tend to generate the long-wave Pacific-North America (PNA) "arching pattern" (Wallace and Gutzler 1981). However, the PNA pattern is dynamically possible only at zonal waves 1-3 (Hoskins and Karoly 1981). The filtered result therefore highlights shorter-wave responses that are sensitive to midlatitude forcing terms such as the transient vorticity, divergence and temperature balances – i.e. processes that are crucial in the CGT maintenance (Schubert et al. 2011).

Exploring the relationship of the 2010 Pakistan floods with climate change, Wang et al. (2011b) found that the 32-year trend in the upper-level divergent circulation exhibited a distinct short-wave feature. Figure 1a depicts such a feature, delineated by the linear trend of the 250-hPa geopotential height in July for the period 1979-2010. Furthermore, the trend in the short-wave component (i.e. filtered with zonal wave-5 and beyond) is significant along the jet stream. Such a character contrasts with circulation trends in some other months, such as March (Fig. 1b), which exhibit a dominant long-wave pattern with mostly insignificant short-wave components. Thus, we performed the zonal harmonic (Fourier) analysis on the horizontal distribution of linear trends of the 250-hPa streamfunction during 1979-2010; this identifies the amplitude of each zonal wavenumber (waves 1 to 7), leading to a wave spectrum. The spectrum was calculated for each month within a 10°-latitude zone starting 80°-70°S through 70°-80°N. The 250-hPa streamfunction was used here instead of geopotential height in order to depict circulations features in the tropics with weak pressure gradients.

Our analysis was conducted first using the individual reanalysis and then, the ensemble of the four reanalyses. Figure 2 shows the zonal spectra of trends in streamfunction from the ensemble reanalyses at each 10° latitudinal zone; the results of individual reanalyses are shown in the Supplemental Figure. To depict a dominant short-wave response, which more likely reflects the CGT forcing rather than the ENSO-PNA forcing, the amplitude of the combined zonal waves 4-7 was compared against the amplitude of combined waves 1-3. If the amplitude of each of waves 4-7 was larger that that of waves 1-3, the corresponding latitude zone was highlighted (light blue). For these latitude zones with predominant short-wave spectrums to be highlighted, they must appear consistently in all the reanalyses, in order to minimize spurious trends.

In the Northern Hemisphere (Fig. 2), the seasons that feature a pronounced short-wave variability include summer (June-August), late autumn (October-December) and the month of April. Although short-wave variability is noticeably large in February and May, it does not exceed the magnitude of longer waves. The robust CGT pattern in July (Fig. 1a) is reflected by the dominant amplitude of zonal wave 5 around 40°-50°N, while the weak CGT signal in March (Fig. 1b) is evidenced by the dominant amplitude in waves 1-2. In the Southern Hemisphere, pronounced short-wave variability is distributed more evenly throughout the year than in the Northern Hemisphere, possibly because the jet stream is less seasonally variable. Noteworthy in the Southern Hemisphere is the rather large discrepancy in the short-wave regime among the four reanalyses (Supplemental Figure) owing to the sparse observations in the Southern Hemisphere. Different assimilation procedures that are sensitive to the sparse observations could also play a role. For instance, CFSR depicts stronger short waves than ERA-Interim, while JRA25 and MERRA appear to be between CFSR and ERA-Interim in terms of the number of short-wave regimes. Such a discrepancy results in a conservative (smaller) number of short-wave regimes being picked up by the ensemble mean.

b. Constructing the Circulation Trend Index – $\boldsymbol{\Psi}$ *(psi)*

Given the observed and modeling evidence of an enhanced CGT pattern in the changing climate, we next examined the association between monthly precipitation and circulation anomalies by quantifying the connection between this association and the general circulation's 32-year trend. The quantification involved seven steps, which are illustrated in Fig. 3 to facilitate the explanation. These seven steps may seem complicated, but they are essentially a series of regression and correlation analyses applied on the temporal/spatial dimension of the circulation and precipitation fields.

The quantification begins first by detrending both the monthly 250-hPa streamfunction (*S*) and the monthly precipitation (P), denoted as *S*' and P' (*Step 1*); this step eliminates the possibility of spurious trends in the data, especially P. The detrending was performed using a least-squares regression. The horizontal *S*' was then regressed point-wise on P' (which is an average of four grid points consisting of a 5°x5° domain); this produced a series of one-point regression maps of *S*' corresponding to each 5°x5° domain of P' (*Step 2*). Next, we computed the linear trending pattern of *S*, such as that shown in Fig. 1 (*Step 3*). The regression maps from *Step 2* are then correlated with the *S* trend through a spatial correlation analysis. The resulting correlation coefficient is denoted as $\rho_{PS,S}$ *(Step 4).* Interpretation of $\rho_{PS,S}$ is provided in Section 4a.

As previously mentioned, regional precipitation anomalies are closely associated with the poleward moisture fluxes representing the LLJ. Taking the U.S. Central Plains for example, the LLJ contributes to more than one-third of the total water vapor during the warm season (Helfand and Schubert 1995; Higgins et al. 1997). The LLJ also influences the precipitation variations worldwide, while its strength is modulated by synoptic systems (Stensrud 1996). Thus, to depict the LLJ and its association with the tropospheric circulation, we used the column water vapor flux (**Q**). By subjecting **Q** to the Laplace inverse transform, one can compute the moisture flux streamfunction, S_Q

$$S_Q = \nabla^{-2}(\vec{k} \cdot \nabla \times \mathbf{Q}) \tag{1}$$

and from there, obtain the rotational and divergent components of **Q**,

$$\vec{Q}_R = (Q_R \vec{i} + Q_R \vec{j}) = \left(-\frac{\partial S_Q}{\partial \theta}\vec{i} + \frac{1}{\cos\theta}\frac{\partial S_Q}{\partial \lambda}\vec{j}\right), \tag{2}$$

where λ and θ are longitude and latitude (Chen et al. 1996). Since moisture is concentrated in the lower troposphere, S_Q generally resembles the lower-tropospheric circulation. Further, since the CGT structure is barotropic, i.e. vertically uniform (Branstator 2002), we analyzed S_Q in conjunction with the upper-level streamfunction (S) to detect the tropospheric circulation anomalies that satisfy this structure. Following the approach for constructing $\rho_{PS,S}$ (*Steps 1-4*), the detrended S_Q was then regressed upon P'; the regression pattern corresponding to each P' grid box was then subjected to a spatial correlation analysis. In this case the resulting spatial correlation is denoted $\rho_{PQ,Q}$ (*Step 5*). We next computed the spatial correlation between the regression map of S' and P' and the regression map of S_Q' and P', denoted $\rho_{PS,PQ}$ (*Step 6*). This step quantified the correspondence (or coupling) between synoptic short waves and the LLJ circulation, as required in the CGT framework.

Using these regression/correlation factors, a unitless index was developed to assess the extent to which S (upper-tropospheric circulation) is coupled with S_Q (lower-tropospheric circulation and moisture flux) and their association with P', as well as their correspondence with the circulation trends. We refer to this index as the Circulation Trend Index ($\boldsymbol{\Psi}$ – for wave function), derived empirically as

$$\Psi = (\rho_{PS,S} + \rho_{PQ,Q}) * 0.5 * \rho_{PS,PQ} \quad (3)$$

At any given 5°x5° domain, $\boldsymbol{\Psi}$ represents the degree of consistency between (a) the regression patterns of S' and S_Q' with the precipitation anomalies and (b) the 30-year trends of S and S_Q, weighted by the degree of coupling between the upper-level circulations and the moisture fluxes (*Step 7*). Moreover, in order to detect the short-wave signal we also computed $\boldsymbol{\Psi}$ using spatially filtered S and S_Q (i.e. removing zonal waves 0-3). The resulting index for the short-wave regime is denoted $\boldsymbol{\Psi_S}$. Since the CGT is a midlatitude phenomenon, the analysis was confined to the latitudes of 20°-60° in both hemispheres. Interpretation of $\boldsymbol{\Psi_S}$ is provided in Section 4.

The function $\boldsymbol{\Psi_S}$, as well as the impact of short-wave regime on the circulation anomalies, is illustrated by calculating the root-mean-square (RMS) of $\rho_{PS,S}$ across each 5° latitude band for each month (Fig. 4). To avoid arid regions, only grid points with monthly precipitation amounts greater than 2 mm/day were analyzed here. In the Northern Hemisphere (Fig. 4a), the difference in $\rho_{PS,S}$ between the total and short-wave regimes was significant at the 90% confidence level (ANOVA test), but did not exceed the 99% level. On the other hand, the difference between the RMS of $\boldsymbol{\Psi}$ and $\boldsymbol{\Psi_S}$ (Fig. 4b) was considerably larger, exceeding the 99.9% confidence level. Such a difference highlights the importance of (a) the coupling between moisture flux and upper-level circulation in the short-wave regime (or the CGT) and (b) the profound association between the changing CGT pattern and regional precipitation anomalies. A similar analysis for the Southern Hemisphere (Figs. 4c and 4d) shows that the difference in $\rho_{PS,S}$ between the total and short-wave regimes was insignificant (not exceeding the 90% confidence level), yet the difference between $\boldsymbol{\Psi}$ and $\boldsymbol{\Psi_S}$ was again significant at the 99.9% level. Hereafter, then, we focus on $\boldsymbol{\Psi_S}$ given its greater variability and correspondence with the regional precipitation anomalies.

4. The $\boldsymbol{\Psi_S}$ Diagnosis

a. Examples for interpretation

To substantiate the implications of $\rho_{PS,S}$ and $\boldsymbol{\Psi_S}$, three recent extreme precipitation events are demonstrated here, including the June 2008 “Midwest floods” in the central United States, the April 2011 tornado outbreaks in the southeast United States, and the December 2010 “Queensland floods” in eastern Australia. Shown in Fig. 5a are the anomalous circulations for the June 2008 “Midwest floods” in terms of the short-wave regime 250-hPa streamfunction (*S*250, of zonal waves 4 and beyond) and the rotational component of the water vapor flux ($\boldsymbol{Q}_R$). A zonally elongated short-wave train is present across 40°N, forming a cyclonic cell in the Western U.S. accompanied by the enhanced Great Plains LLJ, revealed by the southerly $\boldsymbol{Q}_R$. Such a circulation coupling reflects the classic “dynamical pattern” that is conducive to rainstorms (Uccellini and Johnson 1979; Johns 1993). Meanwhile, Fig. 5b shows the regression patterns of the detrended S250 and $\boldsymbol{Q}_R$ with the detrended precipitation in the Central Plains (averaged within the domain 95°-90°W, 37°-42°N) using the ensemble precipitation data. A wave train is predominant across 40°N and it is in-phase with the June 2008 anomalies, indicating that the June 2008 circulation pattern satisfies the common synoptic setting for above-normal precipitation in the Midwest. Previous studies (e.g., Karnauskas et al. 2008; Weaver and Nigam 2008) have also found similar wave trains that cause abnormal wet/dry spells in this region. Furthermore, the linear trends in S250 and $\boldsymbol{Q}_R$ over the 1979-2010 period (Fig. 5c) reveal a wave train that resembles both the regression pattern and the 2008 anomaly, suggesting that wet conditions in the Midwest similar to those in June 2008 may have become more common in the changing CGT pattern, further enhancing recent events.

By comparison, patterns of the long-wave regime (zonal waves 1-3; Fig. 6) corresponding to those in Fig. 5 are not consistent. The June 2008 circulation anomalies (Fig. 6a) do not feature any noticeable long-wave pattern over North America; this is in contrast with the marked, continental-scale cyclonic anomaly revealed in the regression pattern (Fig. 6b), which indicates an enhanced jet stream over the Midwest. During the past 32 years, however, there has been a mild trend towards anticyclonic circulations over much of North America (Fig. 6c). Together, these results indicate that June precipitation in the Midwest is increasingly modulated by a consistent CGT pattern rather than any systematic long-wave pattern; this also illustrates the better depiction of $\boldsymbol{\Psi_S}$ over $\boldsymbol{\Psi}$, as was shown in Fig. 4b.

In the second example – the spring of 2011 – we examined the record tornado outbreaks across the southeastern U.S. and flooding in the north. The short-wave regime $S250$ and $\boldsymbol{Q}_R$ in April 2011 (Fig. 7a) show a wave train that echoes the “dynamical pattern,” with a quasi-stationary synoptic trough over the western U.S. and an intensified LLJ over the southern plains (vectors). The regression maps of detrended $S250$ and $\boldsymbol{Q}_R$ with detrended precipitation (averaged over 90°-85°W, 35°-40°N) also reveal a wave train (Fig. 7b) that is in-phase with that of April 2011. Remarkably, the linear trends in $S250$ and $\boldsymbol{Q}_R$ during the period 1979-2010 (Fig. 7c; i.e. excluding 2011) again depict a wave train resembling both that of April 2011 and the regression pattern (this resemblance is quantified by $\boldsymbol{\Psi}_S$ in Section 4b). Recall that a predominant CGT signal was revealed along 50°N in April (Fig. 2). However, in the long-wave regime (not shown) the anomalous circulations do not reveal any coherence between the 2011, regression, and trending patterns. Thus, the marked correspondence among Figs. 7a-c suggests that the abnormality of extreme weather in April 2011 may be part of a long-term change involving the CGT.

Finally, Fig. 8 presents an example for the Southern Hemisphere. Beginning in December, 2010 through January 2011, eastern Australia underwent a series of rainstorms followed by devastating floods, resulting in the so-called “Queensland flood.” The short-wave regime $S250$ and $\boldsymbol{Q}_R$ during December 2010 (Fig. 8a) again depict a short-wave train along the jet stream, with a cyclonic cell protruding over northeast Australia coupled with poleward anomalies of the water vapor fluxes. The regression patterns (Fig. 8b) between precipitation in eastern Australia (147.5°-152.5°E, 30°-20°S) and the detrended $S250$ and $\boldsymbol{Q}_R$ show a similar deepening of the trough west of Queensland connected to the short-wave train; the similarity between Figs. 8a and 8b suggests a CGT linkage of this and past above-normal precipitation events. While strong La Niña conditions during 2010-11 have been linked to the extreme precipitation resulting in the Queensland floods (Evans and Boyer-Souchet 2012), Fig. 8b clearly indicates that the CGT played a role. The wave train also resembles the circulation anomaly associated with the Indian Ocean Dipole (IOD) during austral spring (Cai et al. 2011), though the precipitation response to the IOD is located further south over coastal southeastern Australia (in New South Wales and Victoria) rather than in Queensland. Nevertheless, the trending patterns of $S250$ and $\boldsymbol{Q}_R$ during 1979-2009 (excluding 2010 here for significance test) reveal a short-wave pattern (Fig. 8c) that is in-phase with the regression and the 2010 patterns along the midlatitudes. These results reinforce the proposed connection between enhanced precipitation in eastern-central Australia and long-term changes to the CGT.

b. $\boldsymbol{\Psi_S}$ indication of precipitation change

The horizontal distribution of $\boldsymbol{\Psi_S}$ is shown in Fig. 9, derived from the ensembles of precipitation and reanalyses at a 5° grid spacing. For brevity, and to focus on the seasons that exhibit a pronounced CGT signal, only the warm season (April-August) is shown. Color codes reflect significant $\boldsymbol{\Psi_S}$ while the significance is determined as $p < 0.1$ in all of the correlations ($\rho_{PS,S}$, $\rho_{PQ,Q}$ and $\rho_{PS,PQ}$); insignificant values are presented as gray dots. Arid regions with monthly precipitation less than 2 mm/day are omitted. The analysis was performed over the period 1979-2010. As shown in Fig. 9, a waveform pattern is revealed from the $\boldsymbol{\Psi_S}$ distributions with positive and negative regions alternating about every 30° in longitude. In April, positive $\boldsymbol{\Psi_S}$ values over the U.S. Central Plains and northwest of the Appalachian Mountains correspond with the large precipitation anomalies that occurred in 2011 associated with the record tornado outbreaks in the southeastern U.S.; this reflects the correspondence between the different circulation patterns shown in Fig. 7.

Through June, large positive $\boldsymbol{\Psi_S}$ persists in the U.S. central and northern plains, reflecting the strong coincidence between the regression pattern and the trending pattern (Fig. 5b, c). Previous studies (Cook et al. 2008; Pryor et al. 2009) have observed an increase in late-spring precipitation over the northern plains accompanied by increased southerly winds and moisture flows. Such a pattern suggests that excessive precipitation in May-June 2008 over the Upper Midwest – and again in spring 2010 and 2011 (see e.g., http://water.weather.gov/precip/) – is consistent with a long-term circulation trend involving the CGT. The positive $\boldsymbol{\Psi_S}$ pattern in the U.S. reverses in July and August, with negative values in the northern plains and positive values in the southern plains. The feature is consistent with the July circulation trend in Fig. 1a, showing an anticyclonic cell over the northwestern U.S. which suppresses summer convective storms (e.g., Chen and Newman 1998). Although the present analysis is not intended to depict drought, negative values of $\boldsymbol{\Psi_S}$ do represent enhanced dry conditions associated with the CGT's tendency. The 2011 severe drought in Texas was, in part, linked to the preceding La Niña that induced the PNA long-wave pattern not detectable in the CGT framework. Nonetheless, over the southern plains positive $\boldsymbol{\Psi_S}$ do reflect the two consecutive wet Julys in 2009 and 2010 in Texas, and partial wet conditions in southern Texas in 2007. Wet and dry anomalies in the southern Great Plains are known to respond to ENSO, which itself is uncorrelated with the CGT (Branstator 2002; Ding and Wang 2005) and therefore may not be depicted by the $\boldsymbol{\Psi_S}$ diagnosis. Caution should also be taken when interpreting the result as heavy precipitation in the southern and southeastern coastal regions is influenced by hurricane activity that may not be linked to the CGT.

In Europe and Asia, the $\boldsymbol{\Psi_S}$ diagnosis reveals several features coincident with recent events. Strong negative $\boldsymbol{\Psi_S}$ values over the United Kingdom during the month of May (Fig. 9) are coincident with, and could be an indication of, consecutive heat waves/dry spells in Britain as was the case in 2011 and 2012. An east-west elongated band of positive $\boldsymbol{\Psi_S}$ over East Asia in June, is in agreement with an observed and projected intensification of the Meiyu rainband (Kusunoki et al. 2011). Moreover, negative $\boldsymbol{\Psi_S}$ over western Russia in June-August accompanies recent heat waves in 2010 and again in 2012. The 2010 Russian heat wave has been linked to short Rossby waves that also impacted the 2010 Pakistan flooding (Hong et al. 2011; Wang et al. 2011b; Lau and Kim 2012); that flooding was partly attributable to record extreme precipitation during July in northern Pakistan and corresponds to positive $\boldsymbol{\Psi_S}$ there.

The $\boldsymbol{\Psi_S}$ diagnosis for the Southern Hemisphere is presented in Fig. 10. For brevity we show only the warm season of December, January and March in which the CGT signal prevails (Fig. 2). Positive values of $\boldsymbol{\Psi_S}$ (i.e. wet conditions) over northern and northeastern Australia reflect not only the "Queensland flood" of December 2010 (Fig. 8) but also the observed expansion of the monsoon rainforests due to increased monsoon rains (Bowman et al. 2010). Moreover, positive $\boldsymbol{\Psi_S}$ that cluster in southeastern Brazil during December and January appear to be connected with the severe floods there in January 2011, since heavy rainfall in that region has a known association with short Rossby waves extending between the South Pacific and South America (Junquas et al. 2012).

c. On severe weather

The $\boldsymbol{\Psi_S}$ diagnosis can be applied in the examination of changes in severe weather conditions and their linkage with a changing circulation pattern. The analysis here involves the frequency of precipitation extremes, hail and gusty winds, and tornadoes. However, such records of hail and tornadoes are highly influenced by population density and societal developments, making their trend analysis tentative (Anderson et al. 2007). The use of $\boldsymbol{\Psi_S}$ overcomes this hurdle because it applies detrended variables for regression analysis (*Step 1* in Fig. 3) and only considers the trend in the circulation pattern (*Step 3*).

We focused on the coterminous United States where comprehensive records of severe weather are available. For the assessment of precipitation extremes, we adopted a simple measure by counting the days in which the grid-scale precipitation of the CPC data exceeds the 95% threshold of its probability density function, yielding an extreme precipitation frequency (F). By regressing F upon the short-wave regime $S250$ and ψ_Q, one obtains $\rho_{FZ,Z}$ and $\rho_{FQ,Q}$ and can use them to derive a new set of $\boldsymbol{\Psi_S}$ with respect to F; that is, repeating the 7-step procedure outlined in Fig. 3.

The result of $\boldsymbol{\Psi_S}$ with respect to F is shown in Fig. 11a for the warm season of April-August. Overall, the distributions of $\boldsymbol{\Psi_S}$ resemble those derived from monthly precipitation (Fig. 8), with positive values over the northern plains during April-June and negative values in July, accompanied by opposite situations in the southern plains. Previous research (e.g., Kunkel et al. 1999; Pryor et al. 2009) has indicated that trends in the mean precipitation and trends in the precipitation frequency are similar, because increased seasonal amounts are often associated with increased precipitation frequency and/or intensity. Noteworthy are the large values near New York in July. According to the 2009 New York City Natural Hazard Mitigation Plan (http://www.nyc.gov/html/oem/downloads/pdf/hazard_mitigation/ section_3j_flooding_hazard_analysis.pdf), severe summer rainstorms linked to flash floods have increased over the past decade, with the highest increase occurring in July. As shown in Fig. 1a, a distinctive cyclonic cell was situated to the west of the East Coast, signaling increasingly favorable synoptic conditions for convective storms.

Following Eq.(3), computing $\boldsymbol{\Psi_S}$ with respect to the frequencies of hail, gusty winds, and F0-5 tornados reveals a linkage between these phenomena with the changing circulation patterns (Figs. 11b and 11c). By following Wang and Chen (2009), the frequencies of hail and gusty winds were combined into one variable to further assess the link with the changing circulation patterns. The frequency of hail and gusty winds is mostly distributed towards the southern or western periphery of high precipitation areas. This is because warm-season storms, which usually travel eastward and/or northward, produce the maximum convection associated with hails and tornadoes prior to generating the maximum precipitation (Wang and Chen 2009). As is shown in Figs. 11b and 11c, positive $\boldsymbol{\Psi_S}$ with respect to hail, gusty winds and tornados during April covers not only the central plains but also the southern plains, where moisture is transported from the Gulf of Mexico by the LLJ. Positive $\boldsymbol{\Psi_S}$ of tornado frequency over the southeastern U.S. also coincide with the record tornado outbreaks that occurred in April 2011 (not included in this analysis). This correspondence suggests that the extremeness of the April 2011 tornado outbreaks may be part of a long-term trend. During May and June, positive $\boldsymbol{\Psi_S}$ shifts to the northern plains and the Great Plain. In July, positive $\boldsymbol{\Psi_S}$ only appears in the hail and gusty wind frequencies over the southern Great Plains but not in the tornado frequency. Instead, negative $\boldsymbol{\Psi_S}$ of tornado frequency covers the northern plains in correspondence to the decreased extreme precipitation frequency. In August, only mild trends are observed across the U.S.

Two factors are at play in creating such a strong $\boldsymbol{\Psi_S}$ contrast between spring (April-June) and summer (July-August): (a) an increasingly coupled pattern in spring, such as that revealed in Figs. 5c and 7c, in comparison to the increasingly decoupled pattern in summer as was suggested in Fig. 1a; and (b) the intensified Great Plains LLJ in spring versus the weakened LLJ in summer (Cook et al. 2008). For the latter, the weakened LLJ leads to deceased moisture flux convergence in the northern plains while shifting the convergence over to the southern plains, causing corresponding changes in severe weather conditions.

5. Possible cause of the CGT trend

Here we present a modeling attribution analysis for the possible cause(s) of the CGT trend by using the CMIP5 single forcing experiments for the historical period. In Fig. 12a, the observed trend in the July short-wave streamfunction at 250 hPa is closely distributed along the climatological jet stream (isotach of *u* and *v* winds), consistent with the jet waveguide theory. We next computed the linear trends for the simulated streamfunction from the GHG experiment of the CNRM, GISS and CanESM model ensembles over the comparable 32 years (1974-2005), shown in Fig. 12b . Changes in the CGT pattern are clearly discernable in the simulations of all three models, even though each model has its own bias in the jet stream ranging from being too strong (GISS), to reasonable (CNRM), to too weak (CanESM). All three models simulated the intensification of the climatological short waves across North America and the North Atlantic, although only CanESM depicted the Eurasian wave train and only CNRM captured the North Pacific wave train. By contrast, in the Natural experiment (Fig. 12c) the trends in the short-wave regime are universally and considerably weaker than those in the GHG experiment. Similar contrasts were also revealed in June and August (not shown) although the contrast between the GHG and Natural experiments is strongest in July.

The result of this analysis delineates the likely impact of anthropogenic forcing (i.e. GHG) on the perceived changes in the climatological short-wave pattern and the associated CGT effects. It also confirms recent observational studies (Francis and Vavrus 2012; Screen and Simmonds 2013) that the so-called Arctic amplification (as part of the global warming) has amplified short-wave circulations that could lead to enhancement of extreme weather. Rivière (2011) found that climate projections under increased GHG produced a poleward shift of the eddy-driven jets, an intensification and poleward shift of the storm tracks, and a strengthening of the upper-tropospheric baroclinicity. Rivière (2011) also point out that the jet stream would break more easily under increased baroclinicity. However, Barnes and Hartmann (2012) suggest that wave breaking on the poleward flank (cyclonic side) of the jet has already reached its poleward limit and will likely become less frequent if the jet migrates any further with increased GHG loading, in essence stopping the jet from its poleward shift. Therefore, though the results presented in Fig. 12 provide a logical indication that increased GHG loading may result in a weakened and increasingly meandering jet stream, more sophisticated analysis using the full archive of CMIP5 models is necessary to draw a firmer conclusion.

6. Concluding Remarks

What are the implications and value of this $\boldsymbol{\Psi_S}$ formulation for precipitation and extreme weather trends? One benefit is the ability to connect and quantify trends in certain circulation patterns (in this case the CGT) and associated changes in precipitation. Another advantage is the reduction of multiple parameters to a single index, avoiding uncertainties in the trends of precipitation and storm activity (e.g., tornado frequency) trends. The results, as presented here, indicate that $\boldsymbol{\Psi_S}$ captures these trends concisely and ascribes to them a dynamical mechanism; this method may also provide a guideline for predicting extreme climate events, as both the CGT and extreme precipitation events have a strong subseasonal signal (e.g., Wang et al. 2010; Schubert et al. 2011). Although current operational weather/climate prediction models have limited skill in forecasting precipitation, they have shown a reasonable ability in forecasting subseasonal variability of circulations both in the tropics (e.g., Waliser 2005) and in the midlatitudes and associated precipitation extremes (e.g., Jones et al. 2011a). It has been demonstrated that seasonal forecasts of circulation patterns can be applied to predicting precipitation extremes (Jones et al. 2011b) and, with the aid of empirical modeling, small-scale phenomena such as valley temperature inversions (Gillies et al. 2010).

Caution should be exercised when interpreting the $\boldsymbol{\Psi_S}$ results. First, the index does not reflect any long-term change in precipitation, hail, gusty winds or tornados, as those variables have been detrended during the computation. Thus, the diagnoses presented here only apply to precipitation changes that are linked to circulation anomalies relevant to the CGT. For instance, it is known that the U.S. southwest monsoon has intensified in conjunction with increased precipitation amounts and broadened spatial coverage (Anderson et al. 2010). However, this feature is not evident in either the monthly precipitation (Fig. 9) or the precipitation frequency (Fig. 11a) during July and August. Such a discrepancy apparently results from the lack of known connection between the southwest monsoon and the CGT. Second, tropical influences should be taken into account. As shown in Fig. 8, extreme precipitation events tend to occur with deepened and intensified midlatitude troughs extending towards the tropics; this is in contrast to the fact that CGT trends are confined within the jet stream latitudes. The mechanisms of such a deepening and intensification of local circulations are somewhat different case-by-case, requiring further analysis. Finally, the 32-year period beginning in 1979 may be modulated by certain decadal-scale oscillatory modes in either the Pacific or the Atlantic. The selection of post-1979 analysis was merely based on the best possible data coverage and quality of the reanalyses.

Regardless, the $\boldsymbol{\Psi_S}$ diagnosis may provide a useful metric in the evaluation of climate model simulations and projections. $\boldsymbol{\Psi_S}$ as a single index would reveal not only the extent of simulated circulation changes but also the geographical distribution of any associated changes in the precipitation and extremeness. Apart from the application perspective, the $\boldsymbol{\Psi_S}$ diagnosis presented here also illustrates the CGT's importance to midlatitude weather/climate extremes and associated trends. Future work should focus on the exploration of the dynamical mechanisms leading to the different CGT responses in different seasons. Of similar importance is the assessment of climate model projections for possible changes in the CGT.

Acknowledgements

This study was supported by NASA Grant NNX13AC37G and the Agricultural Experiment Station, Utah State University, and approved as journal paper 8542.

References

Adler, R. F., and Coauthors, 2003: The Version-2 Global Precipitation Climatology Project (GPCP) Monthly Precipitation Analysis (1979,ÄìPresent). *Journal of Hydrometeorology*, **4,** 1147-1167.

Ambrizzi, T., B. J. Hoskins, and H.-H. Hsu, 1995: Rossby Wave Propagation and Teleconnection Patterns in the Austral Winter. *J. Atmos. Sci.*, **52,** 3661-3672.

Anderson, B. T., J. Wang, G. Salvucci, S. Gopal, and S. Islam, 2010: Observed Trends in Summertime Precipitation over the Southwestern United States. *J. Climate*, **23,** 1937-1944.

Anderson, C. J., C. K. Wikle, Q. Zhou, and J. A. Royle, 2007: Population Influences on Tornado Reports in the United States. *Wea. Forecasting*, **22,** 571-579.

Archer, C. L., and K. Caldeira, 2008: Historical trends in the jet streams. *Geophys. Res. Lett.*, **35,** L08803.

Barnes, E. A., and D. L. Hartmann, 2012: Detection of Rossby wave breaking and its response to shifts of the midlatitude jet with climate change. *Journal of Geophysical Research: Atmospheres*, **117,** D09117.

Bowman, D. J. S., B. Murphy, and D. Banfai, 2010: Has global environmental change caused monsoon rainforests to expand in the Australian monsoon tropics? *Landscape Ecol*, **25,** 1247-1260.

Branstator, G., 2002: Circumglobal Teleconnections, the Jet Stream Waveguide, and the North Atlantic Oscillation. *J. Climate*, **15,** 1893-1910.

Cai, W., P. Van Rensch, T. Cowan, and H. H. Hendon, 2011: Teleconnection pathways of ENSO and the IOD and the mechanisms for impacts on Australian rainfall. *J. Climate*, **24,** 3910-3923.

Chen, M., P. Xie, J. E. Janowiak, and P. A. Arkin, 2002: Global Land Precipitation: A 50-yr Monthly Analysis Based on Gauge Observations. *Journal of Hydrometeorology*, **3,** 249-266.

Chen, P., and M. Newman, 1998: Rossby Wave Propagation and the Rapid Development of Upper-Level Anomalous Anticyclones during the 1988 U.S. Drought. *J. Climate*, **11,** 2491-2504.

Chen, T.-C., M.-C. Yen, and S. Schubert, 1996: Hydrologic Processes Associated with Cyclone Systems over the United States. *Bull. Amer. Meteor. Soc.*, **77,** 1557-1567.

Cook, K. H., E. K. Vizy, Z. S. Launer, and C. M. Patricola, 2008: Springtime Intensification of the Great Plains Low-Level Jet and Midwest Precipitation in GCM Simulations of the Twenty-First Century. *J. Climate*, **21,** 6321-6340.

Dee, D. P., and Coauthors, 2011: The ERA-Interim reanalysis: configuration and performance of the data assimilation system. *Quarterly Journal of the Royal Meteorological Society*, **137,** 553-597.

Diffenbaugh, N. S., J. S. Pal, R. J. Trapp, and F. Giorgi, 2005: Fine-scale processes regulate the response of extreme events to global climate change. *Proceedings of the National Academy of Sciences of the United States of America*, **102,** 15774-15778.

Ding, Q., and B. Wang, 2005: Circumglobal Teleconnection in the Northern Hemisphere Summer. *J. Climate*, **18,** 3483-3505.

——, 2007: Intraseasonal Teleconnection between the Summer Eurasian Wave Train and the Indian Monsoon. *J. Climate*, **20,** 3751-3767.

Doswell, C. A., 2001: *Severe Convective Storms.* Vol. 28, Ameri. Meteor. Soc., 570 pp.

Easterling, D. R., G. A. Meehl, C. Parmesan, S. A. Changnon, T. R. Karl, and L. O. Mearns, 2000: Climate Extremes: Observations, Modeling, and Impacts. *Science*, **289,** 2068-2074.

Evans, J. P., and I. n. Boyer-Souchet, 2012: Local sea surface temperatures add to extreme precipitation in northeast Australia during La Nina. *Geophy. Res. Lett.*, **39,** L10803.

Francis, J. A., and S. J. Vavrus, 2012: Evidence linking Arctic amplification to extreme weather in mid-latitudes. *Geophy. Res. Lett.*, **39,** L06801.

Gaffen, D. J., B. D. Santer, J. S. Boyle, J. R. Christy, N. E. Graham, and R. J. Ross, 2000: Multidecadal Changes in the Vertical Temperature Structure of the Tropical Troposphere. *Science*, **287,** 1242-1245.

Ghosh, S., V. Luniya, and A. Gupta, 2009: Trend analysis of Indian summer monsoon rainfall at different spatial scales. *Atmospheric Science Letters*, **10,** 285-290.

Gillies, R. R., S.-Y. Wang, J.-H. Yoon, and S. Weaver, 2010: CFS Prediction of Winter Persistent Inversions in the Intermountain Region. *Wea. Forecasting*, **25,** 1211–1218.

Helfand, H. M., and S. D. Schubert, 1995: Climatology of the Simulated Great Plains Low-Level Jet and Its Contribution to the Continental Moisture Budget of the United States. *J. Climate*, **8,** 784-806.

Higgins, R. W., Y. Yao, and X. L. Wang, 1997: Influence of the North American Monsoon System on the U.S. Summer Precipitation Regime. *J. Climate*, **10,** 2600-2622.

Hong, C. Ä., H. Ä. Hsu, N. Ä. Lin, and H. Chiu, 2011: Roles of European blocking and tropical‚Äêextratropical interaction in the 2010 Pakistan flooding. *Geophy. Res. Lett.*, **38**.

Hoskins, B. J., and D. J. Karoly, 1981: The Steady Linear Response of a Spherical Atmosphere to Thermal and Orographic Forcing. *J. Atmos. Sci.*, **38,** 1179-1196.

Hoskins, B. J., and T. Ambrizzi, 1993: Rossby Wave Propagation on a Realistic Longitudinally Varying Flow. *J. Atmos. Sci.*, **50,** 1661-1671.

Johns, R. H., 1993: Meteorological Conditions Associated with Bow Echo Development in Convective Storms. *Wea. Forecasting*, **8,** 294-299.

Jones, C., L. M. V. Carvalho, J. Gottschalck, and W. Higgins, 2011a: The Madden‚ÄìJulian Oscillation and the Relative Value of Deterministic Forecasts of Extreme Precipitation in the Contiguous United States. *J. Climate*, **24,** 2421-2428.

Jones, C., J. Gottschalck, L. M. V. Carvalho, and W. Higgins, 2011b: Influence of the Madden,ÄìJulian Oscillation on Forecasts of Extreme Precipitation in the Contiguous United States. *Mon. Wea. Rev.*, **139,** 332-350.

Junquas, C., C. Vera, L. Li, and H. Treut, 2012: Summer precipitation variability over Southeastern South America in a global warming scenario. *Clim. Dynamics*, **38,** 1867-1883.

Karnauskas, K. B., A. Ruiz-Barradas, S. Nigam, and A. J. Busalacchi, 2008: North American Droughts in ERA-40 Global and NCEP North American Regional Reanalyses: A Palmer Drought Severity Index Perspective. *J. Climate*, **21,** 2102-2123.

Krishnan, R., and M. Sugi, 2001: Baiu Rainfall Variability and Associated Monsoon Teleconnections. *Journal of the Meteorological Society of Japan*, **79,** 851-860.

Kunkel, K. E., K. Andsager, and D. R. Easterling, 1999: Long-Term Trends in Extreme Precipitation Events over the Conterminous United States and Canada. *J. Climate*, **12,** 2515-2527.

Kusunoki, S., R. Mizuta, and M. Matsueda, 2011: Future changes in the East Asian rain band projected by global atmospheric models with 20-km and 60-km grid size. *Clim. Dynamics*, **37,** 2481-2493.

Lau, K. M., and H. Weng, 2002: Recurrent Teleconnection Patterns Linking Summertime Precipitation Variability over East Asia and North America. *Journal of the Meteorological Society of Japan*, **80,** 1309-1324.

Lau, W. K., and K.-M. Kim, 2012: The 2010 Pakistan flood and Russian heat wave: Teleconnection of hydrometeorological extremes. *Journal of Hydrometeorology*, **13,** 392-403.

Lu, J., C. Deser, and T. Reichler, 2009: Cause of the widening of the tropical belt since 1958. *Geophys. Res. Lett.*, **36,** L03803.

Maddox, R. A., 1980: Mesoscale convective complexes. *Bull. Amer. Meteor. Soc.*, **61,** 1374-1387.

Maddox, R. A., 1983: Large-Scale Meteorological Conditions Associated with Midlatitude, Mesoscale Convective Complexes. *Mon. Wea. Rev.*, **111,** 1475-1493.

Matsueda, M., 2011: Predictability of Euro-Russian blocking in summer of 2010. *Geophys. Res. Lett.*, **38,** L06801.

Monaghan, A. J., D. L. Rife, J. O. Pinto, C. A. Davis, and J. R. Hannan, 2010: Global Precipitation Extremes Associated with Diurnally Varying Low-Level Jets. *J. Climate*, **23,** 5065-5084.

O'Gorman, P. A., and T. Schneider, 2009: The physical basis for increases in precipitation extremes in simulations of 21st-century climate change. *Proc. Natl. Acad. Sci.*, **106,** 14773-14777.

Onogi, K., and Coauthors, 2007: The JRA-25 Reanalysis. *Journal of the Meteorological Society of Japan. Ser. II*, **85,** 369-432.

Paltridge, G., A. Arking, and M. Pook, 2009: Trends in middle- and upper-level tropospheric humidity from NCEP reanalysis data. *Theoretical and Applied Climatology*, **98,** 351-359.

Pryor, S. C., J. A. Howe, and K. E. Kunkel, 2009: How spatially coherent and statistically robust are temporal changes in extreme precipitation in the contiguous USA? *Inter. J. Climatol.*, **29,** 31-45.

Rienecker, M. M., and Coauthors, 2011: MERRA - NASA's Modern-Era Retrospective Analysis for Research and Applications. *J. Climate***, 24**, 3624-3648.

Rivière, G., 2011: A Dynamical Interpretation of the Poleward Shift of the Jet Streams in Global Warming Scenarios. *J. Atmos. Sci.*, **68,** 1253-1272.

Saha, S., and Coauthors, 2010: The NCEP Climate Forecast System Reanalysis. *Bull. Amer. Meteor. Soc.*, **91,** 1015-1057.

Schubert, S., H. Wang, and M. Suarez, 2011: Warm season subseasonal variability and climate extremes in the Northern Hemisphere: The role of stationary Rossby waves. *J. Climate*, **24,** 4773–4792.

Screen, J. A., and I. Simmonds, 2013: Exploring links between Arctic amplification and mid-latitude weather. *Geophy. Res. Lett.***,** n/a-n/a.

Seidel, D. J., Q. Fu, W. J. Randel, and T. J. Reichler, 2008: Widening of the tropical belt in a changing climate. *Nature Geosci*, **1,** 21-24.

Stensrud, D. J., 1996: Importance of Low-Level Jets to Climate: A Review. *J. Climate*, **9,** 1698-1711.

Sugiyama, M., H. Shiogama, and S. Emori, 2010: Precipitation extreme changes exceeding moisture content increases in MIROC and IPCC climate models. *Proc. Natl. Acad. Sci.*, **107,** 571-575.

Sun, Y., S. Solomon, A. Dai, and R. W. Portmann, 2007: How Often Will It Rain? *J. Climate*, **20,** 4801-4818.

Taylor, K. E., R. J. Stouffer, and G. A. Meehl, 2011: An Overview of CMIP5 and the Experiment Design. *Bull. Amer. Meteor. Soc.*, **93,** 485-498.

Tetzlaff, G., J. Zimmer, and R. Faulwetter, 2012: Extreme Rain Events in Mid-Latitudes. *Environmental Hazards: The Fluid Dynamics and Geophysics of Extreme Events*, H. K. Moffatt, Ed., National University of Singapore, 193-228.

Uccellini, L. W., 1980: On the Role of Upper Tropospheric Jet Streaks and Leeside Cyclogenesis in the Development of Low-Level Jets in the Great Plains. *Mon. Wea. Rev.*, **108,** 1689-1696.

Uccellini, L. W., and D. R. Johnson, 1979: The Coupling of Upper and Lower Tropospheric Jet Streaks and Implications for the Development of Severe Convective Storms. *Mon. Wea. Rev.*, **107,** 682-703.

Waliser, D. E., 2005: Predictability and forecasting. *Intraseasonal Variability in the Atmosphere-Ocean Climate System*, K. M. Lau, and D. E. Waliser, Eds., Springer, 389-423.

Wallace, J. M., and D. S. Gutzler, 1981: Teleconnections in the Geopotential Height Field during the Northern Hemisphere Winter. *Mon. Wea. Rev.*, **109,** 784-812.

Wang, S.-Y., and T.-C. Chen, 2009: The Late-Spring Maximum of Rainfall over the U.S. Central Plains and the Role of the Low-Level Jet. *J. Climate*, **22,** 4696-4709.

Wang, S.-Y., T.-C. Chen, and E. Takle, 2011a: Climatology of summer midtropospheric perturbations in the US northern plains. Part II: large-scale effects of the Rocky Mountains on genesis. *Clim. Dynamics*, **36,** 1221-1237.

Wang, S.-Y., R. E. Davies, W.-R. Huang, and R. R. Gillies, 2011b: Pakistan's two-stage monsoon and links with the recent climate change. *J. Geophy. Res.*, **116,** D16114.

Wang, S.-Y., L. E. Hipps, R. R. Gillies, X. Jiang, and A. L. Moller, 2010: Circumglobal teleconnection and early summer rainfall in the US Intermountain West. *Theor. Appl. Climatol.*, **102,** 245-252.

Weaver, S. J., and S. Nigam, 2008: Variability of the Great Plains Low-Level Jet: Large-Scale Circulation Context and Hydroclimate Impacts. *J. Climate*, **21,** 1532-1551.

Weaver, S. J., S. Schubert, and H. Wang, 2009: Warm Season Variations in the Low-Level Circulation and Precipitation over the Central United States in Observations, AMIP Simulations, and Idealized SST Experiments. *J. Climate*, **22,** 5401-5420.

Weiss, S., Hart, JA, Janish, PR 2002: An examination of severe thunderstorm wind report climatology. *21st Conf. on Severe Local Storms*.

Xie, P., and P. A. Arkin, 1997: Global Precipitation: A 17-Year Monthly Analysis Based on Gauge Observations, Satellite Estimates, and Numerical Model Outputs. *Bull. Amer. Meteor. Soc.*, **78,** 2539-2558.

Yasui, S., and M. Watanabe, 2010: Forcing Processes of the Summertime Circumglobal Teleconnection Pattern in a Dry AGCM. *J. Climate*, **23,** 2093-2114.

Zipser, E. J., C. Liu, D. J. Cecil, S. W. Nesbitt, and D. P. Yorty, 2006: WHERE ARE THE MOST INTENSE THUNDERSTORMS ON EARTH? *Bull. Amer. Meteor. Soc.*, **87,** 1057-1071.

Figure Captions

Fig. 1 Linear trends in the 250-hPa eddy geopotential height (with the zonal mean removed; contours) and the spatially filtered geopotential height with zonal waves 1-4 removed (shadings) for (a) July and (b) March during 1979-2010, using the 4-reanalysis ensemble. Shadings exceeding +7 and -7 m are significant ($p<0.05$).

Fig. 2 Wave spectrums of the linear trends in the 250-hPa streamfunction spanning zonal waves 1-7 within a 10° latitude zones for each month. Analysis period is 1979-2010; data source is the 4-reanalyses ensemble. Light blue shadings indicate the latitude zones where the short-wave spectrums (waves 4-7 combined) were larger than the long-wave spectrums (waves 1-3). The Y-scale is fixed in all months and all latitude zones.

Fig. 3 Flow charts depicting the 7 steps in creating the $\mathbf{\Psi}$ index (and $\mathbf{\Psi}_S$ with zonally filtered S and S_Q). See text for details.

Fig. 4 Root-mean-square of $\rho_{PS,\,S}$ (see text and Fig. 3) over each 5 latitude degree zonal band in (a) the Northern Hemisphere and (c) the Southern Hemisphere throughout the year. Numbers indicate each individual month; $\rho_{PS,\,S}$ computed from the eddy streamfunction (i.e. with the zonal mean removed) are shown in blue and marked as *Eddy*, while that computed from the short-wave regime are shown in red and marked as *SW*. (b) and (d) Same as (a) and (c) but for the Ψ in blue and Ψ_S in red.

Fig. 5 (a) Anomalous patterns of the short-wave filtered 250-hPa streamfunction (S250; shadings) and rotational moisture fluxes ($\mathbf{Q}_R$; vectors) during June 2008 the "Midwest flood." (b) Patterns of June S250 and $\mathbf{Q}_R$ regressed upon the precipitation anomalies averaged over the Midwest (blue box) for the period of 1979-2010; all variables were detrended. (c) Linear trends in *S*250 (shadings) and $\mathbf{Q}_R$ (vectors) over the period of 1979-2010.

Fig. 6 Same as Fig. 5 but for the long-wave filtered fields (zonal waves 1-3). The blue box in (b) indicates where the precipitation anomalies were used to construct the regression map.

Fig. 7 Same as Fig. 5 but for April and for (a) the 2011 tornado outbreaks in the southeastern United

States. The blue box in (b) indicates where the precipitation anomalies were used to construct the regression map.

Fig. 8 Same as Fig. 5 but for December in the Southern Hemisphere and for (a) the 2010 "Queensland floods" in Australia, for the period of 1979-2009 (excluding year 2010 to provide an independent assessment). The blue box in (b) indicates where the precipitation anomalies were used to construct the regression map.

Fig. 9 Horizontal distributions of Ψ_S for the months indicated atop each panel. Color dots reflect the significant values and gray dots are insignificant. Areas in which the monthly precipitation is smaller than 2 mm/day are omitted.

Fig. 10 Same as Fig. 9 but for the Southern Hemisphere.

Fig. 11 Same as Fig. 9 but showing the Ψ_S derived from (a) precipitation frequency of which the grid-scale precipitation exceeds the 95% threshold of its probability density function, (b) frequency of hails and gusty winds combined, and (c) frequency of F0-5 tornadoes over the United States.

Fig. 12 Linear trends of the July 250-hPa streamfunction at the zonal waves 5 regime (shadings) overlaid with the jet stream (contours of wind speed), derived from (a) the 4-reanalysis ensemble, (b) each of the 3 models of the GHG experiment, and (c) the 3 models of the Natural experiment. Shadings in all panels exceeding 8 and -8 x $10^5 m^2 s^{-1}$ are significant ($p<0.05$).

SI Figure: Same as Fig. 2 but for each of the four reanalyses.

Table 1 Global reanalysis, precipitation datasets, and CMIP5 models used

Name	Full Name & Agency	Spatial Resolution
MERRA	Modern-Era Retrospective Analysis for Research and Applications, by the National Aeronautics and Space Administration (NASA)	1.0° long. x lat. extrapolated to 2.5°
ERA-Interim	ECMWF Interim Reanalysis Project, by the European Centre for Medium-Range Weather Forecasts (ECMWF)	1.5° long. x lat. → extrapolated to 2.5°
CFSR	Climate Forecast System Reanalysis, by the National Oceanic and Atmospheric Administration (NOAA)	2.5° long. x lat.
JRA-25	Japanese 25-year ReAnalysis, by the Japan Meteorological Agency (JMA)	2.5° long. x lat.
GPCP	Global Precipitation Climatology Project v2, by NASA	2.5° long. x lat.
CMAP	Climate Prediction Center Merged Analysis of Precipitation, by NOAA	2.5° long. x lat.
GPCC	Global Precipitation Climatology Centre v4	1.0° long. x lat. extrapolated to 2.5°
PREC/L	NOAA's Precipitation Reconstruction over Land	1.0° long. x lat. extrapolated to 2.5°
CPC	Climate Prediction Center's Daily Unified precipitation in U.S.	0.5° long. x lat.
GISS	NASA's Goddard Institute for Space Studies (GISS) model	~2.0° long. x lat.
CNRM	Centre National de Recherches Météorologiques – CM5 version	~2.0° long. x lat.
CanESM	The Canadian Earth System Model	~1.25° long. x lat.

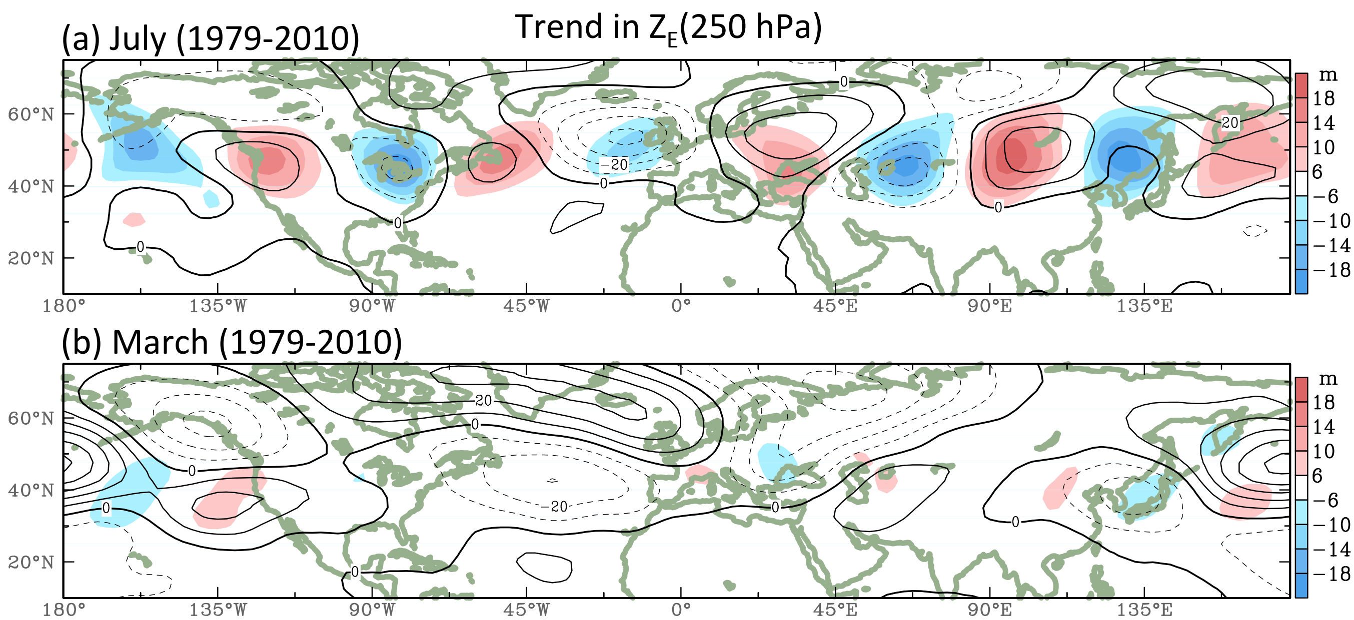

Fig. 1 Linear trends in the 250-hPa eddy geopotential height (with the zonal mean removed; contours) and the spatially filtered geopotential height with zonal waves 1-4 removed (shadings) for (a) July and (b) March during 1979-2010, using the 4-reanalysis ensemble. Shadings exceeding +7 and -7 m are significant ($p<0.05$).

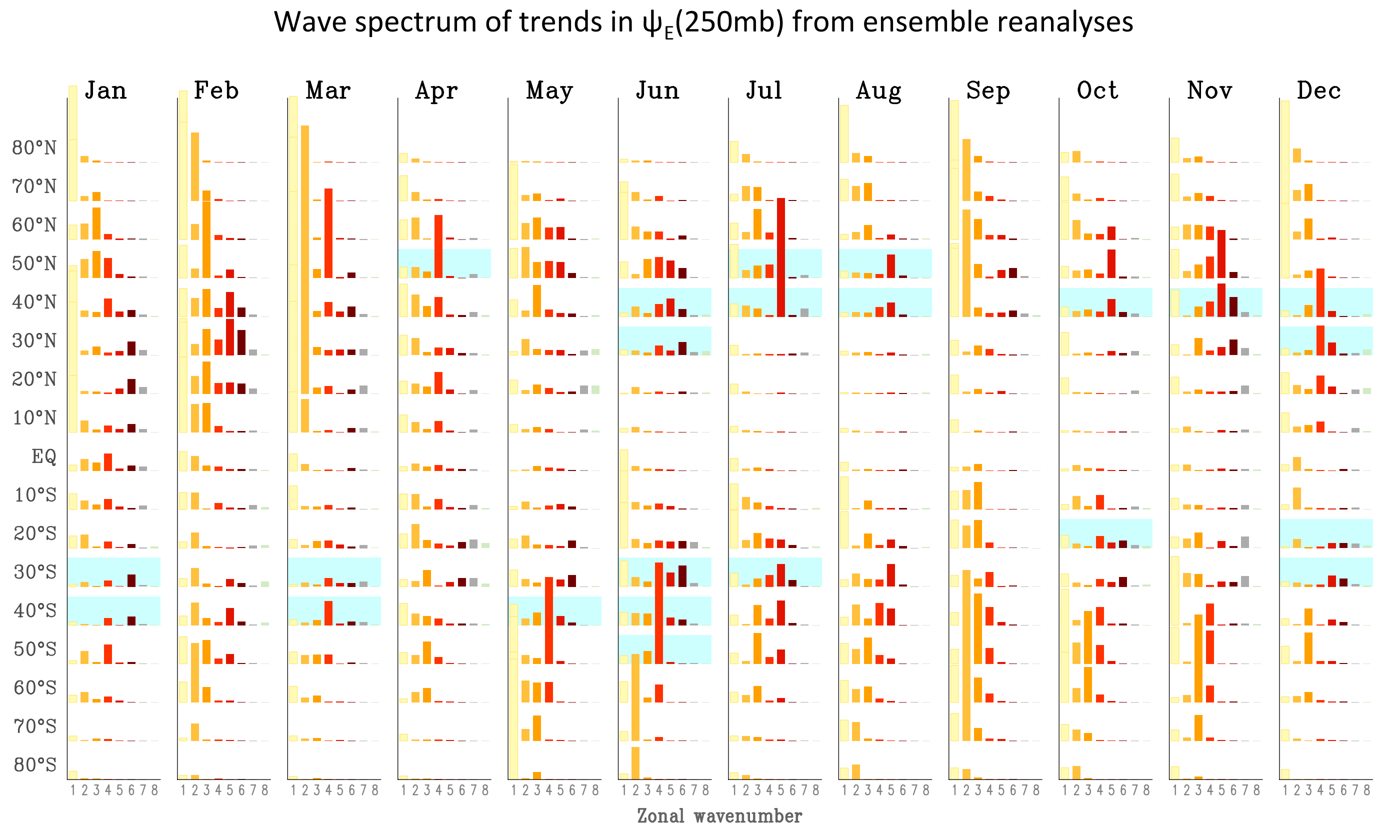

Fig. 2 Wave spectrums of the linear trends in the 250-hPa streamfunction spanning zonal waves 1-7 within a 10° latitude zones for each month. Analysis period is 1979-2010; data source is the 4-reanalyses ensemble. Light blue shadings indicate the latitude zones where the short-wave spectrums (waves 4-7 combined) were larger than the long-wave spectrums (waves 1-3). The Y-scale is fixed in all months and all latitude zones.

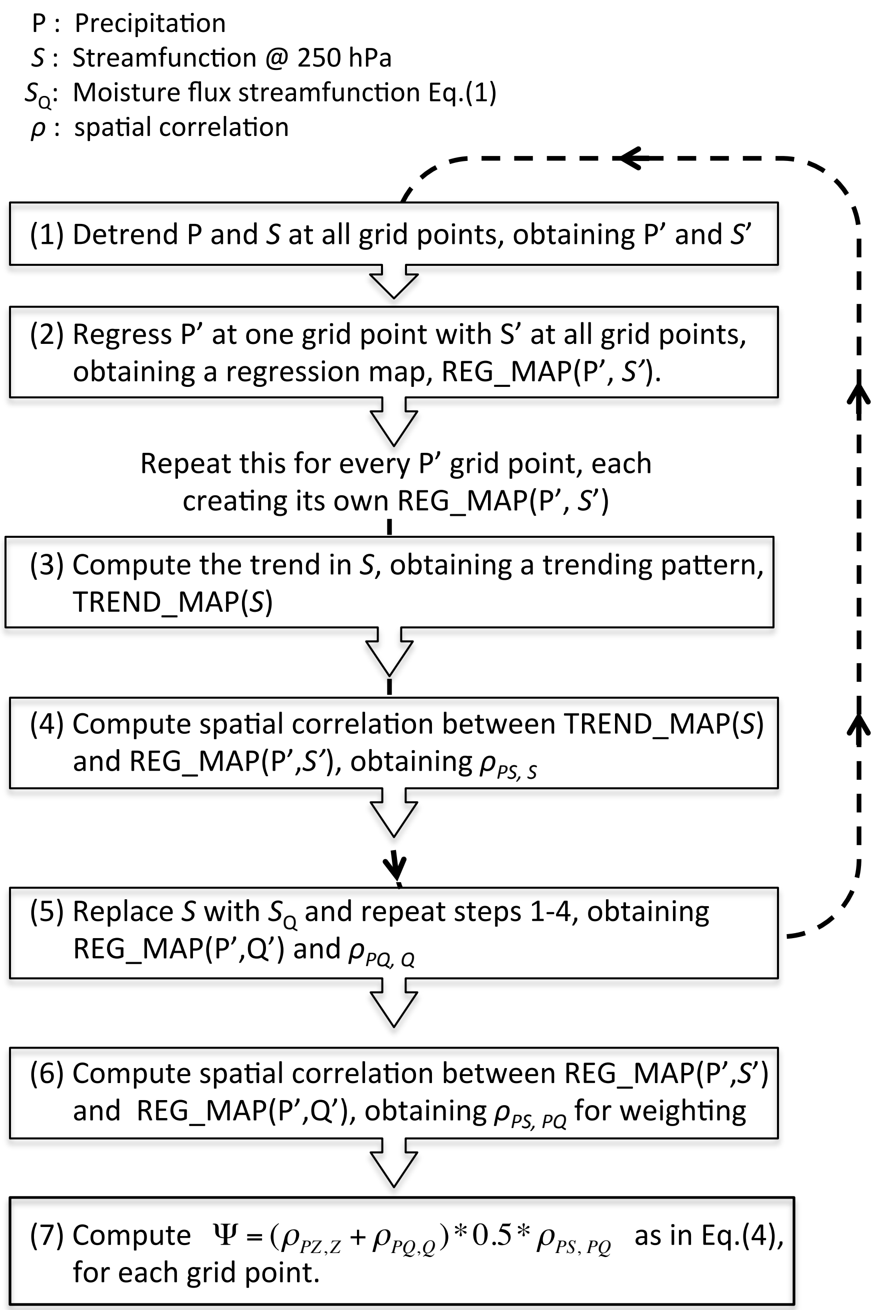

Fig. 3 Flow charts depicting the 7 steps in creating the **Ψ** index (and $\mathbf{\Psi}_S$ with zonally filtered S and S_Q). See text for details.

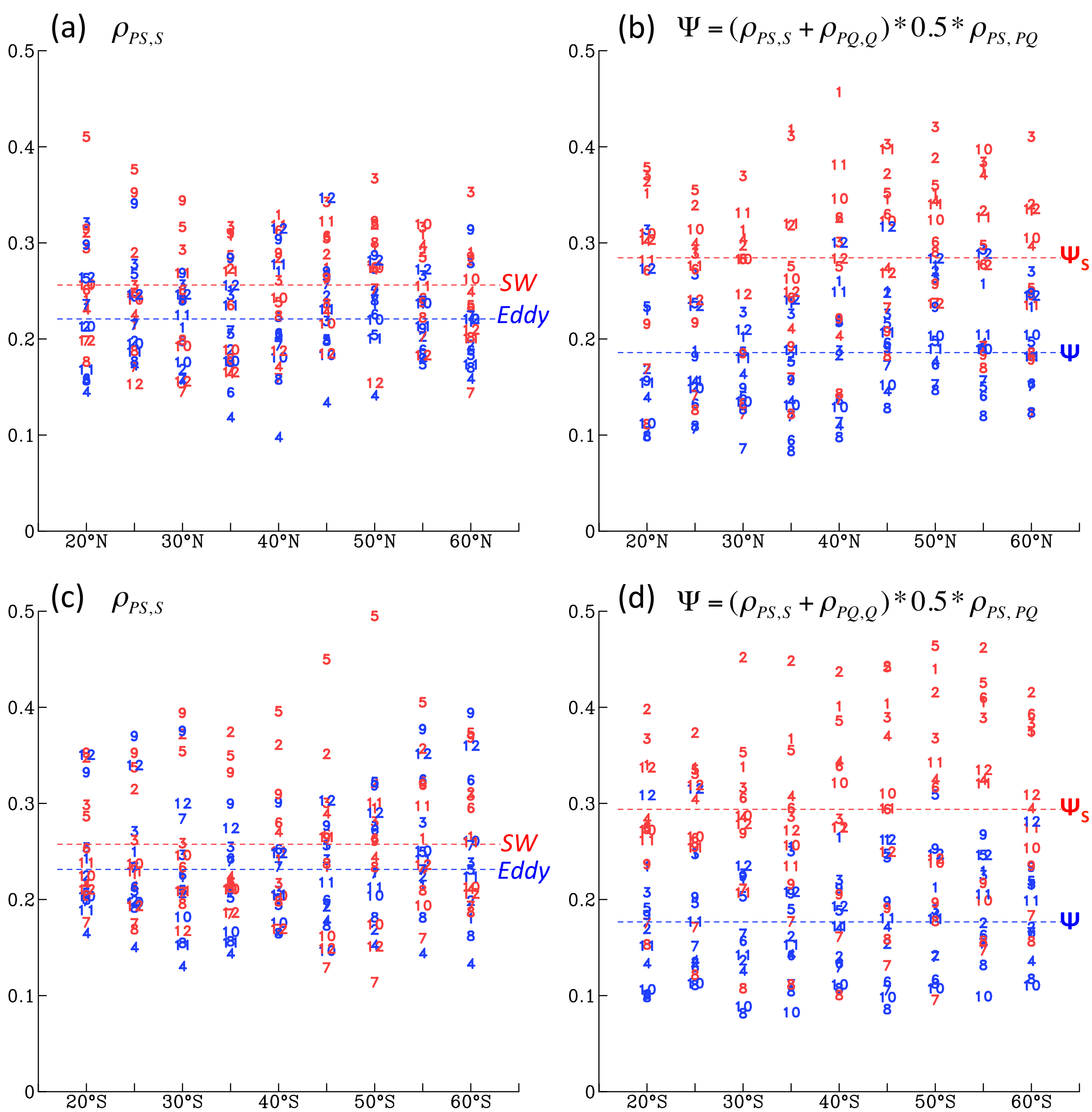

Fig. 4 Root-mean-square of $\rho_{PS,S}$ (see text and Fig. 3) over each 5 latitude degree zonal band in (a) the Northern Hemisphere and (c) the Southern Hemisphere throughout the year. Numbers indicate each individual month; $\rho_{PS,S}$ computed from the eddy streamfunction (i.e. with the zonal mean removed) are shown in blue and marked as *Eddy*, while that computed from the short-wave regime are shown in red and marked as *SW*. (b) and (d) Same as (a) and (c) but for the Ψ in blue and Ψ_S in red.

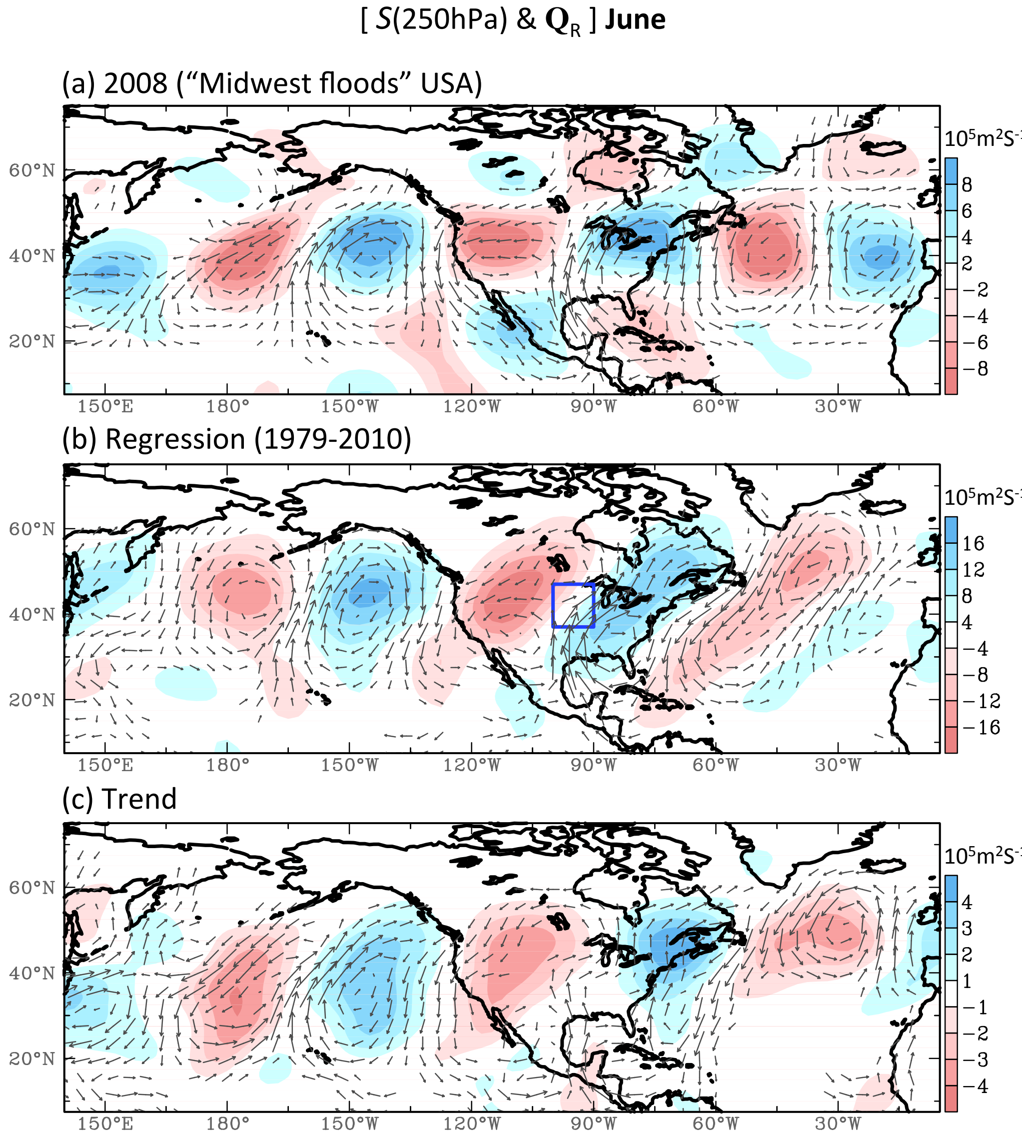

Fig. 5 (a) Anomalous patterns of the short-wave filtered 250-hPa streamfunction (S250; shadings) and rotational moisture fluxes ($\mathbf{Q}_R$; vectors) during June 2008 the "Midwest flood." (b) Patterns of June S250 and $\mathbf{Q}_R$ regressed upon the precipitation anomalies averaged over the Midwest (blue box) for the period of 1979-2010; all variables were detrended. (c) Linear trends in *S*250 (shadings) and $\mathbf{Q}_R$ (vectors) over the period of 1979-2010.

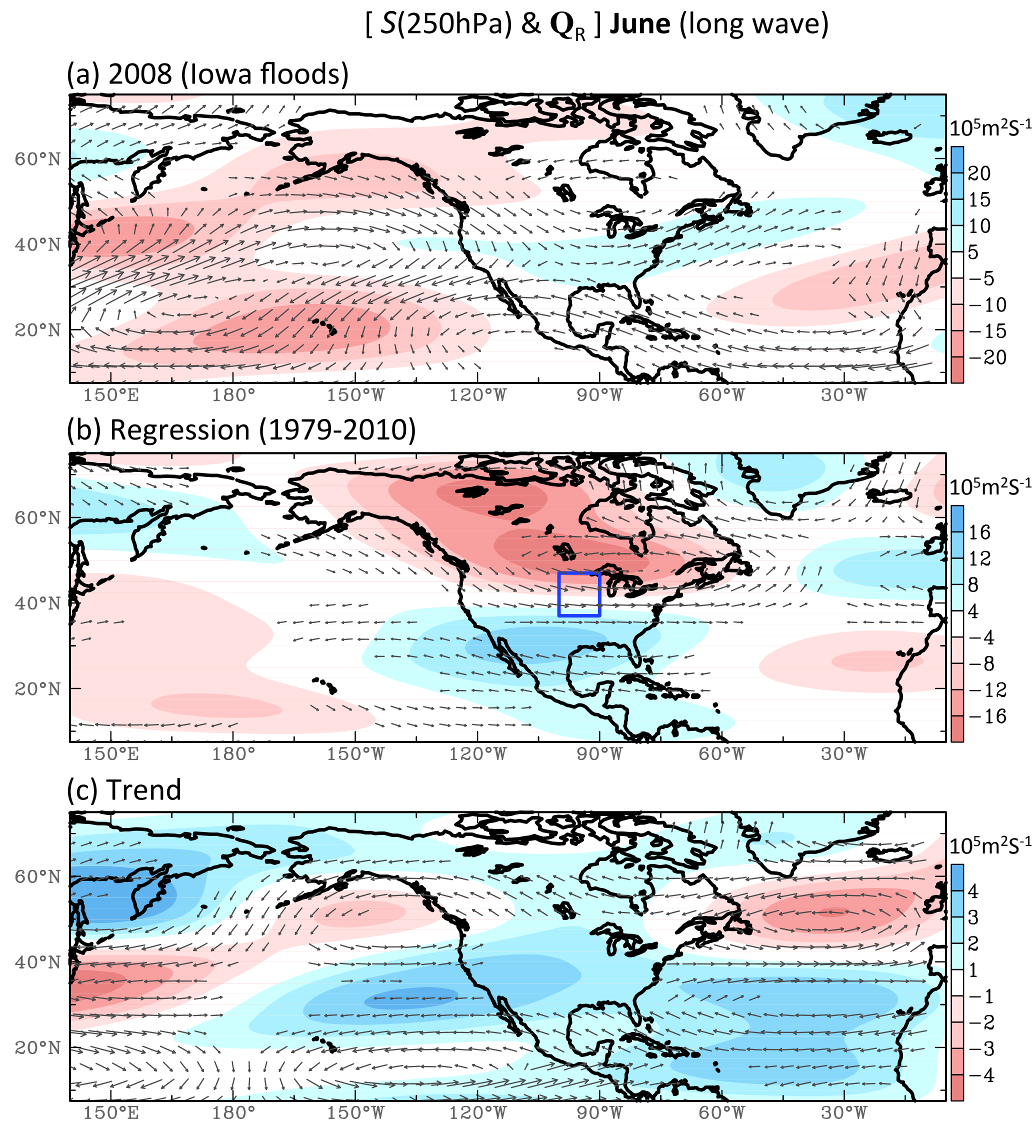

Fig. 6 Same as Fig. 5 but for the long-wave filtered fields (zonal waves 1-3). The blue box in (b) indicates where the precipitation anomalies were used to construct the regression map.

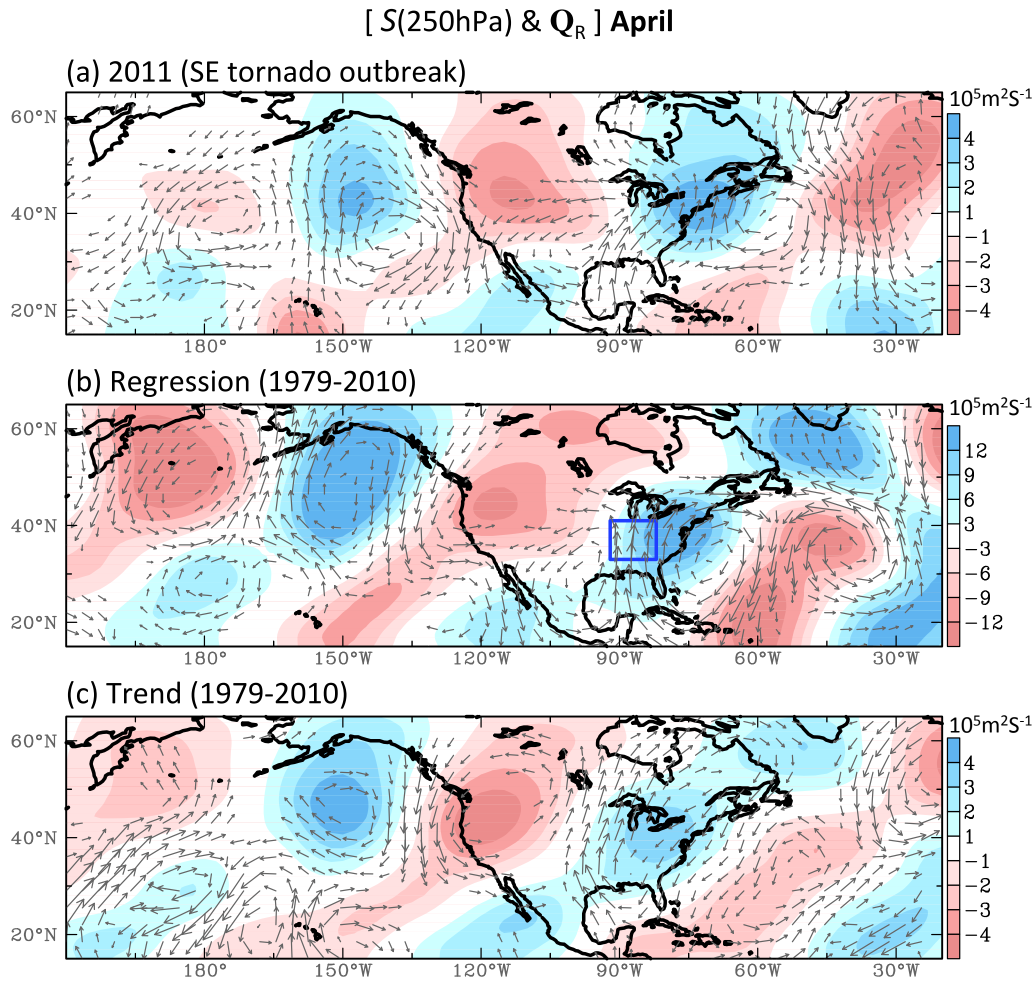

Fig. 7 Same as Fig. 5 but for April and for (a) the 2011 tornado outbreaks in the southeastern United States. The blue box in (b) indicates where the precipitation anomalies were used to construct the regression map.

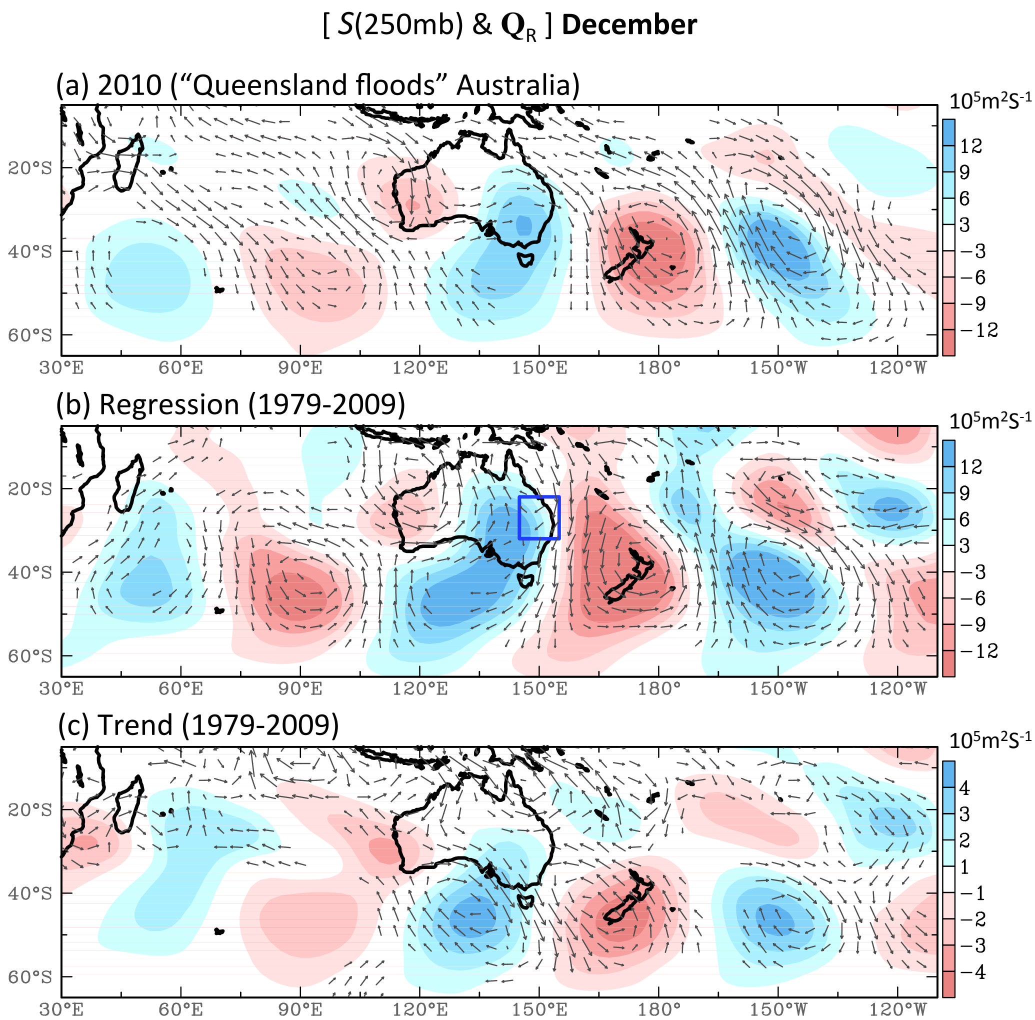

Fig. 8 Same as Fig. 5 but for December in the Southern Hemisphere and for (a) the 2010 “Queensland floods” in Australia, for the period of 1979-2009 (excluding year 2010 to provide an independent assessment). The blue box in (b) indicates where the precipitation anomalies were used to construct the regression map.

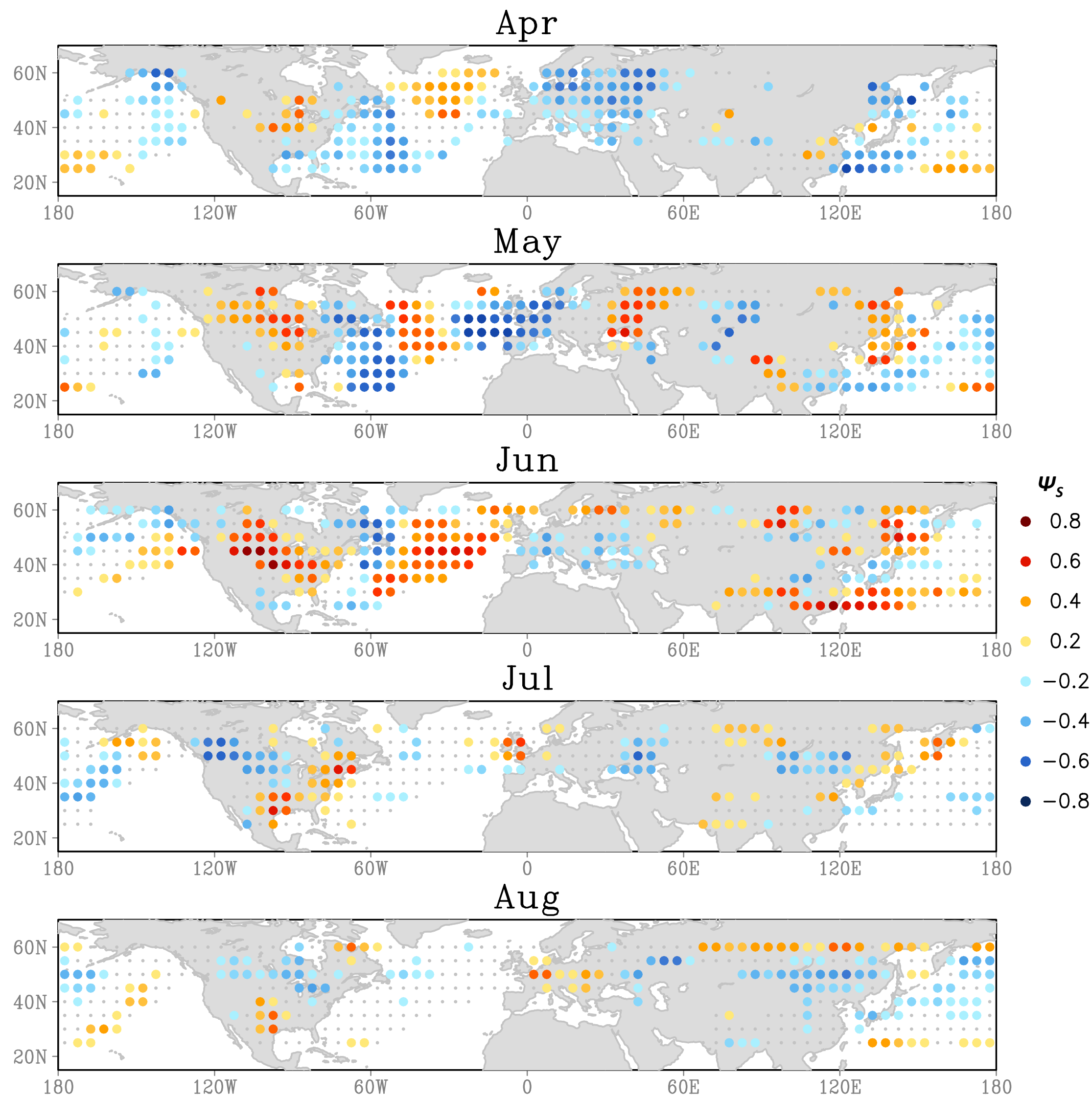

Fig. 9 Horizontal distributions of Ψ_S for the months indicated atop each panel. Color dots reflect the significant values and gray dots are insignificant. Areas in which the monthly precipitation is smaller than 2 mm/day are omitted.

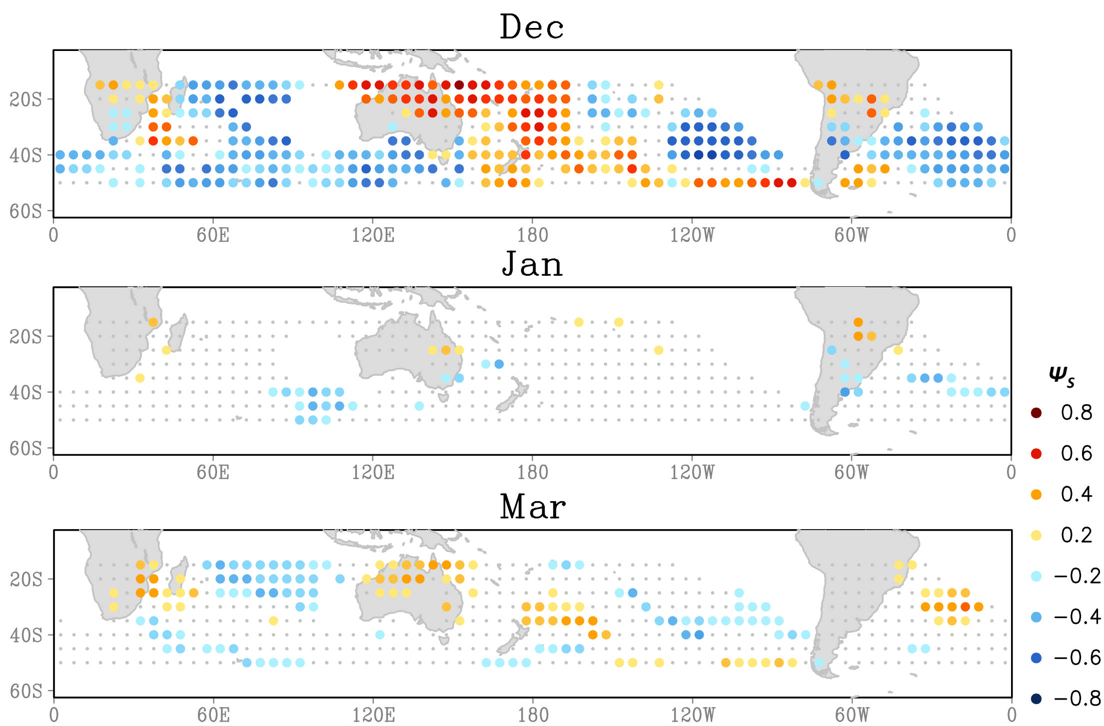

Fig. 10 Same as Fig. 9 but for the Southern Hemisphere.

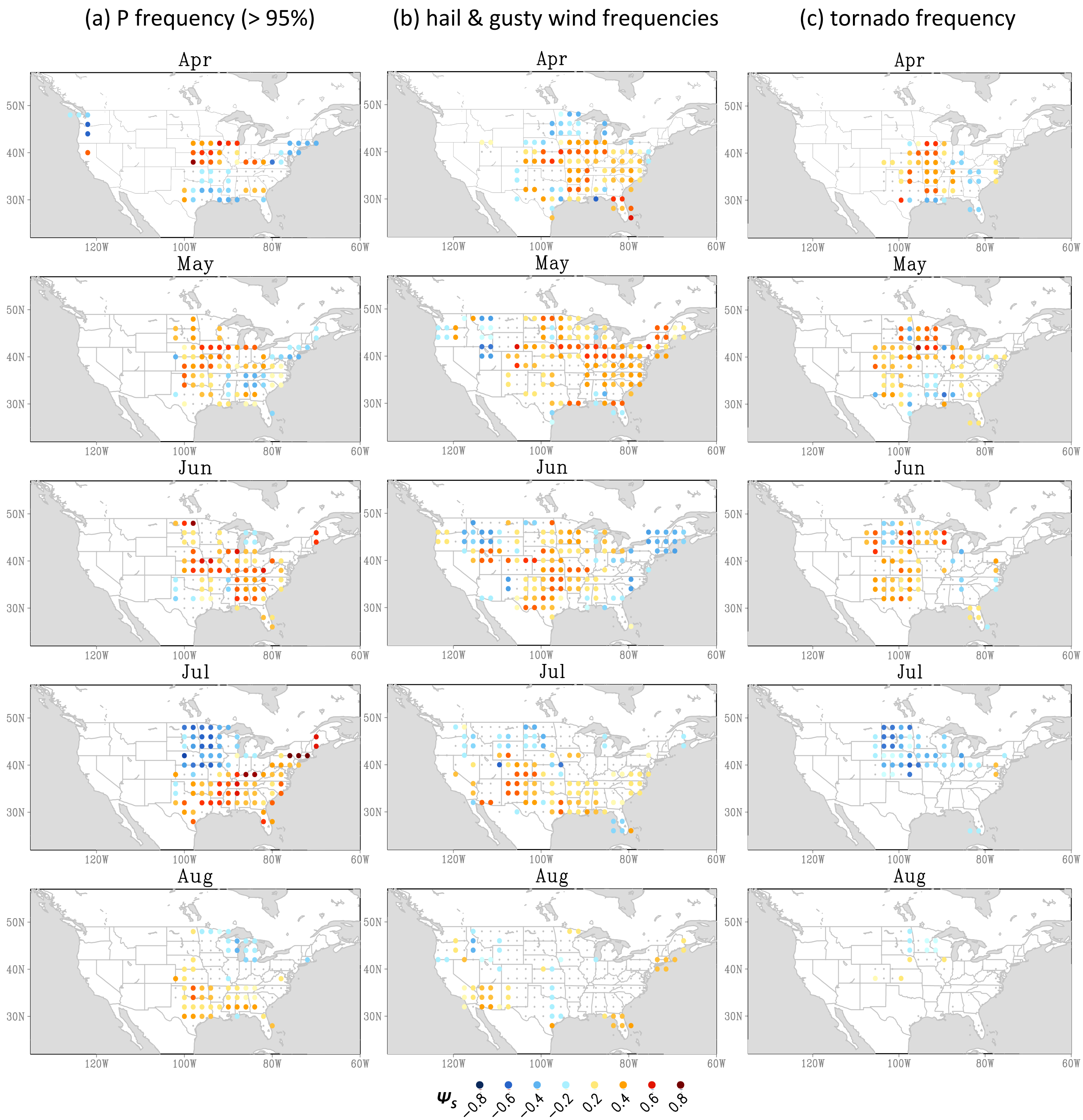

Fig. 11 Same as Fig. 9 but showing the Ψ_S derived from (a) precipitation frequency of which the grid-scale precipitation exceeds the 95% threshold of its probability density function, (b) frequency of hails and gusty winds combined, and (c) frequency of F0-5 tornadoes over the United States.

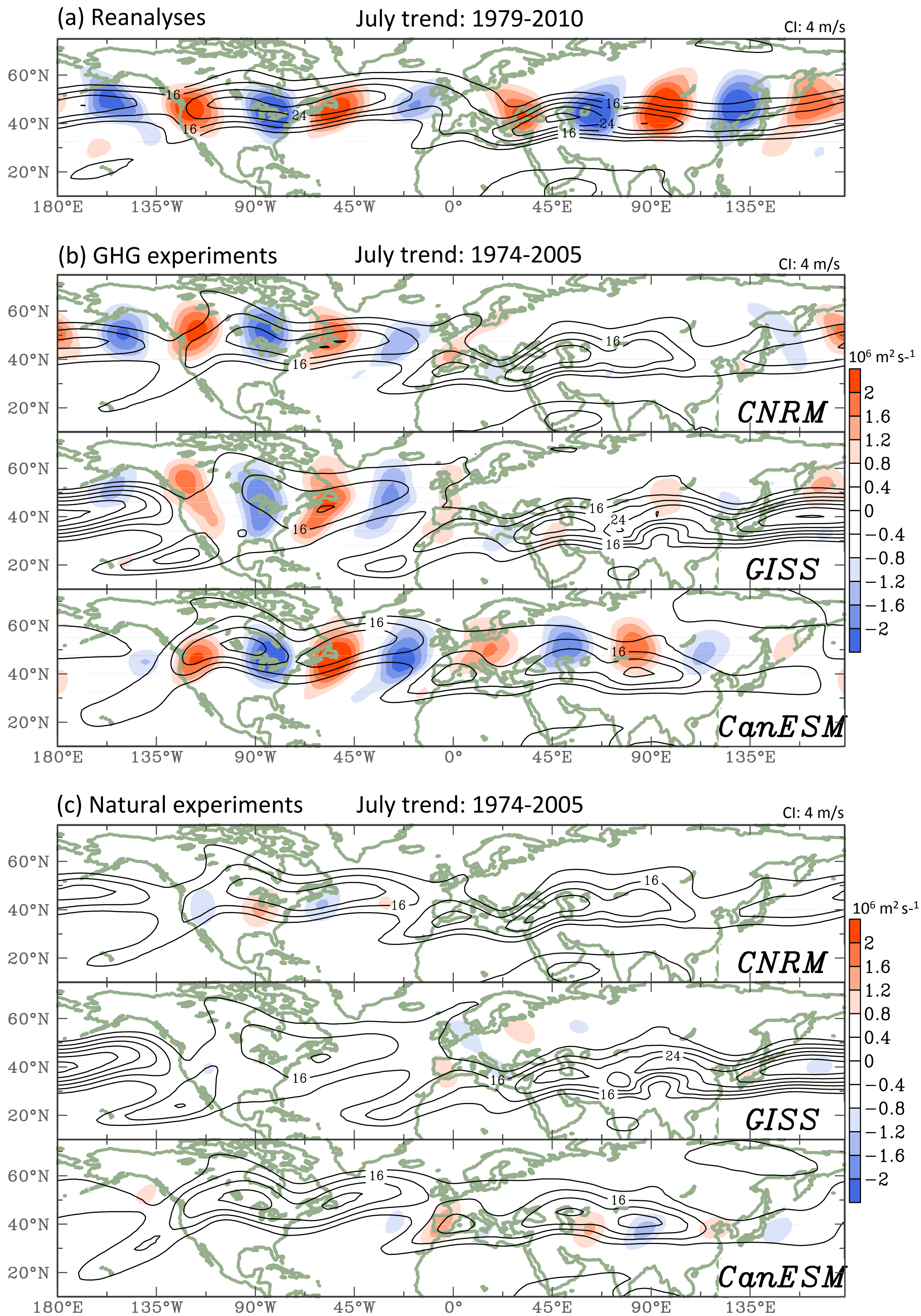

Fig. 12 Linear trends of the July 250-hPa streamfunction at the zonal waves 5 regime (shadings) overlaid with the jet stream (contours of wind speed), derived from (a) the 4-reanalysis ensemble, (b) each of the 3 models of the GHG experiment, and (c) the 3 models of the Natural experiment. Shadings in all panels exceeding 8 and -8 x $10^5 m^2 s^{-1}$ are significant ($p<0.05$).

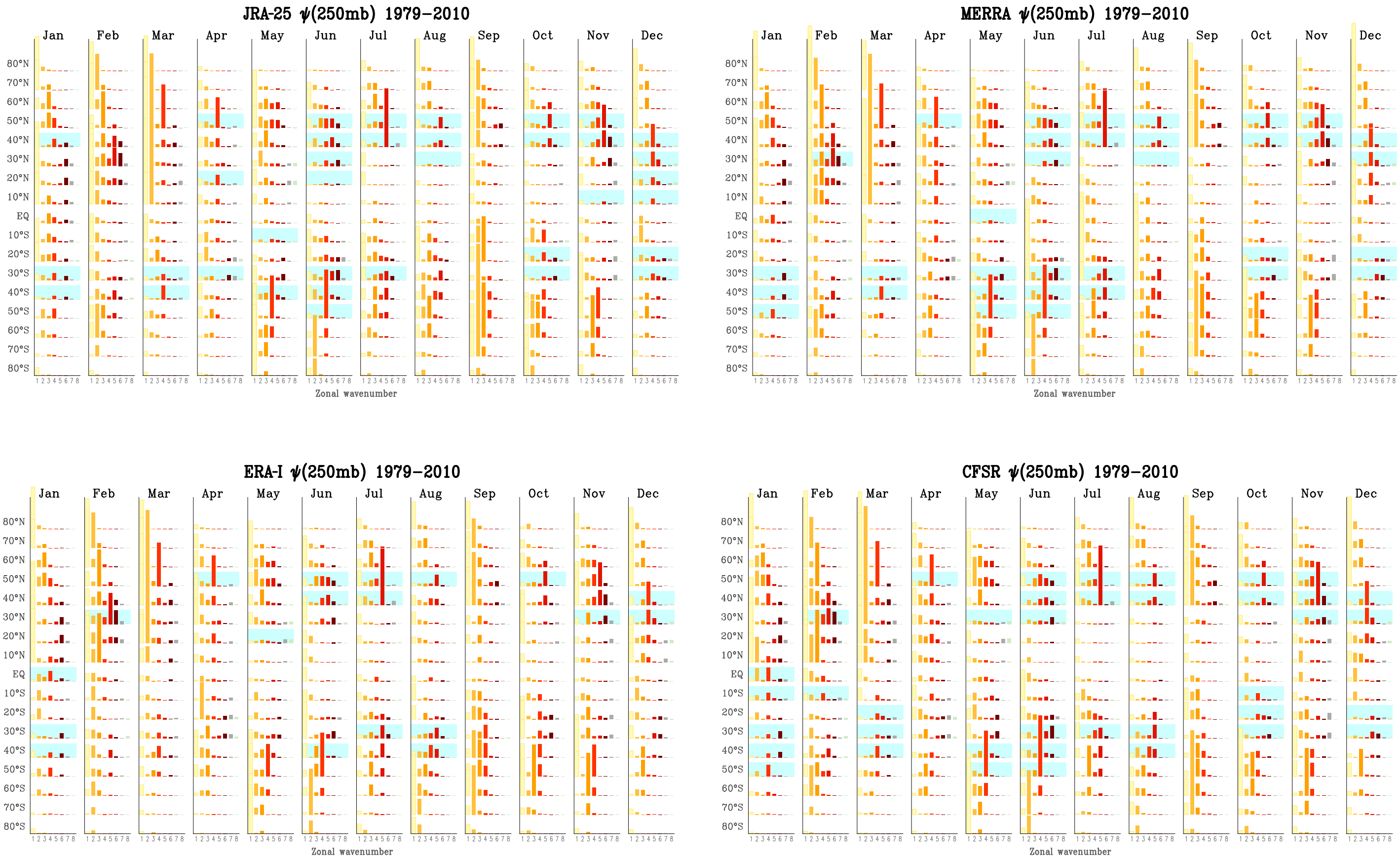

SI Figure: Same as Fig. 2 but for each of the four reanalyses.